ACADEMIC PRESS

Available online at www.sciencedirect.com
SCIENCE DIRECT®

Icarus 164 (2003) 14–32

ICARUS

www.elsevier.com/locate/icarus

The effects of topographically-controlled thermal tides in the martian upper atmosphere as seen by the MGS accelerometer

Paul Withers,[a,*] S.W. Bougher,[b] and G.M. Keating [c]

[a] *Lunar and Planetary Laboratory, University of Arizona, Tucson, AZ 85721, USA*
[b] *Space Physics Research Laboratory, AOSS Department, University of Michigan, 2455 Hayward Avenue, Ann Arbor, MI 48109-2143, USA*
[c] *The George Washington University at NASA Langley, MS 269, Hampton, VA 23681, USA*

Received 4 October 2002; revised 5 February 2003

Abstract

Mars Global Surveyor accelerometer observations of the martian upper atmosphere revealed large variations in density with longitude during northern hemisphere spring at altitudes of 130–160 km, all latitudes, and mid-afternoon local solar times (LSTs). This zonal structure is due to tides from the surface. The zonal structure is stable on timescales of weeks, decays with increasing altitude above 130 km, and is dominated by wave-3 (average amplitude 22% of mean density) and wave-2 (18%) harmonics. The phases of these harmonics are constant with both altitude and latitude, though their amplitudes change significantly with latitude. Near the South Pole, the phase of the wave-2 harmonic changes by 90° with a change of half a martian solar day while the wave-3 phase stays constant, suggesting diurnal and semidiurnal behaviour, respectively. We use a simple application of classical tidal theory to identify the dominant tidal modes and obtain results consistent with those of General Circulation Models. Our method is less rigorous, but simpler, than the General Circulation Models and hence complements them. Topography has a strong influence on the zonal structure.

Keywords: Mars, atmosphere; Tides, atmospheric; Atmospheres, dynamics

1. Introduction

Our objectives in this paper are to understand the nature of large variations in density with longitude observed in the martian upper atmosphere with the Mars Global Surveyor (MGS) accelerometer and to identify the underlying phenomena that cause them. We present a quantitative and detailed analysis of this zonal structure as a function of altitude, latitude, and local solar time (LST). We then use classical tidal theory to identify the dominant mechanisms causing the zonal structure, and finally outline a simple justification for topography having a strong influence on the zonal structure. We begin by quantifying the sol-to-sol (a sol is a martian solar day) variability, or weather, in the martian upper atmosphere and placing some constraints on its origin.

Accelerometer data from MGS's aerobraking phases revealed an unexpected phenomenon: the upper atmospheric density at fixed altitude, latitude, LST, and season varied by factors of 2 or more as a function of longitude (Keating et al., 1998). Corresponding atmospheric variabilities for the Earth, measured by the Satellite Electrostatic Triaxial Accelerometer at its reference altitude of 200 km altitude, are on the order of 10% (Forbes et al., 1999). For reference, typical atmospheric densities at 200 km altitude on Earth in Forbes et al. are $\sim 0.1\ \mathrm{kg\,km^{-3}}$ and typical atmospheric densities at 130 km altitude on Mars in this paper (Tables 2 and 3) are $\sim 1\ \mathrm{kg\,km^{-3}}$. No such variations can be observed on Venus because its similar lengths of day and year do not allow all longitudes to have the same LST on a subannual timescale.

This zonal structure must originate in the lower atmosphere; it cannot be created in situ. There are no zonal inhomogeneities present in solar heating, which powers the dynamics of the martian atmosphere, or in the upper boundary of the atmosphere. There are many zonal inhomogeneities near the lower boundary of the atmosphere, including topography, surface thermal inertia, surface albedo, and lower atmosphere dust loading, which may influence this zonal structure. Since the zonal structure must prop-

* Corresponding author.
E-mail address: withers@lpl.arizona.edu (P. Withers).

0019-1035/03/$ – see front matter
doi:10.1016/S0019-1035(03)00135-0

agate through, and be affected by, the lower atmosphere, observations of the zonal structure in the upper atmosphere may reveal information about the properties of the lower atmosphere. This zonal structure is caused by atmospheric tides, which are global-scale atmospheric oscillations at periods which are subharmonics of a solar day (Forbes, 1995).

"Keating et al. (1998) initially found that the zonal structure intensified during the build-up of a regional dust storm and, based on the constancy of its phasing, suggested that it may be caused by topographically forced stationary waves. Later in the MGS mission measurements were made on the nightside and Keating et al., (1999, 2000) detected a phase reversal of wave-2 from day to night which they attributed to non-migrating tides (specifically the diurnal Kelvin wave)" (Keating, 2003, personal communication). Non-migrating tides, disturbances that vary with time but are not locked in phase with the Sun, were also suggested by (Forbes and Hagan, 2000; Joshi et al., 2000; Wilson, 2000; Forbes et al., 2001). They are discussed in Section 5. The restricted sampling in LST of the accelerometer data make these two types of disturbances impossible to distinguish observationally. Stationary waves are unlikely because they require an implausible vertical profile of zonal winds in the lower atmosphere if they are to be present in the upper atmosphere. All of these publications responding to Keating et al. (1998) predate the public release of the accelerometer dataset, hence they are based on the limited quantitative data presented in that paper and short conference abstracts discussing the complete accelerometer dataset (Keating et al., 1999, 2000). Here we present an analysis of the complete accelerometer dataset.

A previous publication has discussed the properties of the zonal structure, including its responses to changes in altitude, latitude, and LST, using the complete accelerometer dataset. Wilson (2002) observed that the zonal structure decreased in amplitude with increasing altitude and did not change in phase with changes in latitude. Wilson discussed the observation of Withers et al. (2000) that the zonal structure varied with half a sol changes in LST. Wilson did not present quantitative results for how altitude or LST affected the zonal structure, nor did he quantify changes in the zonal structure on weekly timescales. Wilson only presented quantitative results for the strongest two components of the zonal structure, wave-2 and wave-3. In this paper we present quantitative results for all these items, including the first four harmonic components of the zonal structure. Wilson compared his analysis of the MGS density data to GCM predictions that accurately reproduced some aspects of the zonal structure, such as its amplitude and phase at 130 km and its changes with LST. He used them to identify the dominant tides causing the zonal structure. Unlike Wilson (2002), we use our observations in conjunction with idealised classical tidal theory to identify the dominant tides. In this longer paper we were able to go into more quantitative detail about the accelerometer dataset and chose a less rigorous, but simpler, theoretical approach to interpret our observations. We also outline a simple justification for topography, rather than any other surface physical property, being the strongest influence on the zonal structure.

The zonal structure and the tidal modes responsible have also been studied by other instruments onboard MGS, including the thermal emission spectrometer (TES), the Mars Horizon Sensor Assembly, and the Radio Science experiment (Banfield et al., 2000, 2003; Smith et al., 2001a; Murphy et al., 2001; Bougher et al., 2001; Hinson et al., 2001; Tracadas et al., 2001).

The dynamics of the martian upper atmosphere are important for several reasons. Firstly, great cost savings are generated when a spacecraft aerobrakes into orbit around Mars, rather than using chemical propellant. Aerobraking is not possible without an understanding of the upper atmosphere and improvements in this understanding yield greater cost savings. Secondly, theoretical models of the upper atmospheres of Earth and Mars, regions which are very sensitive to changes in solar flux, share many key features. Understanding the upper atmosphere of Mars helps develop and verify these models, which can then be used, for example, to monitor changes in solar flux in the Earth's upper atmosphere, an important measurement for terrestrial climate change. Thirdly, as we shall see later in Section 5.1, the dynamics of the lower and upper atmospheres on Mars are strongly coupled, so by understanding the upper atmosphere we also learn about the lower atmosphere. The publicly available accelerometer dataset from the MGS spacecraft is a rich resource for studying the martian upper atmosphere (Keating et al., 2001a,b). The results of this paper contribute to a better understanding of the dynamics of the martian upper atmosphere.

The remainder of this paper is divided into five parts. Section 2 provides background information on the MGS accelerometer dataset. Section 3 examines short-term variability in the upper atmosphere. Section 4 presents observations of the zonal structure. Section 5 uses tidal theory to identify the phenomena causing the zonal structure. Section 6 concludes.

2. MGS aerobraking

An aerobraking spacecraft, such as Mars Global Surveyor, passes through an atmosphere near the periapsis of its orbit and experiences an aerodynamic force which decreases the energy and semimajor axis of the spacecraft's orbit without the need for significant fuel consumption (French and Uphoff, 1979; Eldred, 1991). Aerobraking has previously been used by Atmospheric Explorer-C and its successors at Earth, the Pioneer Venus Orbiter at Venus, and Magellan at Venus (Marcos et al., 1977; Strangeway, 1993; Croom and Tolson, 1994; Lyons et al., 1995). Aerobraking permits in situ atmospheric studies not possible from a typical spacecraft orbit.

MGS carried an Accelerometer Experiment (Keating et al., 1998, 2001a,b). This accelerometer measured the aerodynamic forces on the spacecraft during an aerobraking pass. The accelerometer readings have been processed to generate a "profile" of atmospheric density along each flight path through the atmosphere (Keating et al., 1998; Cancro et al., 1998; Tolson et al., 1999, 2000; Keating et al., 2001a,b). This information was used by the spacecraft operations team in the hours immediately after the aerobraking pass to plan modifications to MGS's trajectory, changing the altitude of the next periapsis in steps of about 2 km by small expenditures of chemical propellant at apoapsis, to achieve the desired drag without exceeding heating rate thresholds, and guide it safely to the desired mapping orbit. MGS's orbit during aerobraking was near-polar, with an inclination of about 93°, and highly elliptical.

The changing characteristics of MGS's orbit during aerobraking were quite complicated and controlled the data coverage of the accelerometer. As such, they strongly influence the data analysis that we are able to do in Sections 3 and 4. We first discuss the orbital characteristics for the case when periapsis is away from the pole.

A typical aerobraking pass through the atmosphere lasted a few minutes and spanned several tens of degrees of latitude with only small changes in longitude or LST; unlike planetary entry probes or landers, the flight path of MGS through the atmosphere on each aerobraking pass is not close to vertical. On a typical aerobraking pass, latitude has a roughly quadratic dependence on altitude. The maximum altitude at which the accelerometer measured atmospheric density, set by the instrument sensitivity, was approximately 160 km. The minimum altitude at which the accelerometer measured atmospheric density was that of periapsis, typically 110 km. Periapsis altitude was rarely outside 100–120 km. It often changed from one orbit to the next by a kilometre or so in response to the non-spherically symmetric gravitational field of Mars, in addition to any deliberate trajectory modifications. As aerobraking progressed, MGS's apoapsis altitude steadily decreased and the parabolic aerobraking pass through the atmosphere became flatter. A given altitude level was crossed twice on each aerobraking pass, once descending towards periapsis at one latitude and longitude, and once ascending after periapsis at another latitude and longitude. To distinguish between these two measurements at the same altitude and same orbit, we refer to the "inbound" and "outbound" legs of an aerobraking pass.

Since the near-polar orbit was close to sun-synchronous, periapsis LST changed only slowly between orbits. Periapsis longitude changed greatly between orbits as the planet rotated every 24.6 h beneath MGS's orbit. The change in periapsis longitude per orbit, relative to 360°, was equal to the ratio of MGS's orbital period to the martian rotational period.

Periapsis latitude changed slowly but steadily between orbits. Due to the oblateness of Mars, the orbit precessed around in its orbital plane (Murray and Dermott, 1999). This caused periapsis latitude to change. The entire parabolic flight path also shifted in latitude as the orbit precessed. Due to this precession, we can analyse densities at a range of altitudes, but fixed latitudes, from the non-vertical aerobraking passes (Section 4.3) and analyse densities at a range of latitudes, but fixed altitudes (Section 4.4). To summarize, MGS had a slowly flattening, parabolic flight path through the atmosphere, travelled in either a north or south direction with small changes in LST and longitude during a pass, with large changes in longitude due to the planet's rotation, small changes in LST, and steady changes in latitude between periapses.

The picture is more complicated when periapsis is in the polar regions. This is discussed in Section 4.5.

Aerobraking took place in two Phases, 1 and 2, separated by a hiatus containing the Science Phasing Orbits (Albee et al., 1998, 2001). Phase 1 included orbits 1–201 from mid-September, 1997, to late March, 1998, and Phase 2 included orbits 574–1283 from mid-September, 1998, to early February, 1999. This covers a range of martian seasons. L_s, martian heliocentric longitude, is 0° at the northern spring equinox, 90° at the northern summer solstice, 180° at the northern autumn equinox, and 270° at the northern winter solstice. At the beginning of Phase 1, $L_s = 180°$, periapsis occurred at 30°N and 18 h LST, then moved northwards and earlier in the day to reach 60°N and 11 h LST at the end of Phase 1, $L_s = 300°$. One "hour" of LST is equal to 1/24th of a sol, not 60 min of elapsed time. MGS flew from north to south through the atmosphere on each aerobraking pass during Phase 1. At the beginning of Phase 2, during the next martian year at $L_s = 30°$, periapsis occurred at 60°N and 17 h LST, then moved southwards and earlier in the day to cross 80°S at 15 h LST. At the beginning of Phase 2, MGS flew from south to north through the atmosphere on each aerobraking pass. Periapsis then reached its furthest south ($\sim 87°$S) near the south pole, crossed the terminator by drifting through nighttime LSTs, and reached 60°S and 02 h LST by the end of Phase 2, $L_s = 90°$. At the end of Phase 2, MGS flew from north to south through the atmosphere on each aerobraking pass. When periapsis was near the south pole, each aerobraking pass's profile of atmospheric density spanned a large range of LST. The behaviour of periapsis during aerobraking is summarised in Fig. 1.

In this paper, we discuss two broad subsets of the accelerometer data, both from Phase 2 of aerobraking. The Phase 1 data are complicated by significant changes in both periapsis latitude and LST between each orbit and by the presence of a regional dust storm, so we leave them for future work. Some work on the Phase 1 data has previously been published (Keating et al., 1998; Bougher et al., 1999). The two subsets of data from Phase 2 are: (1) the southward progression from 60°N to 60°S at almost fixed L_s and LST at the beginning of Phase 2; and (2) the crossing of the south pole from 60°S back to 60°S at almost fixed L_s and two different LSTs, half a sol apart, at the end of Phase 2. We name these two subsets of data the "Daytime Precession"

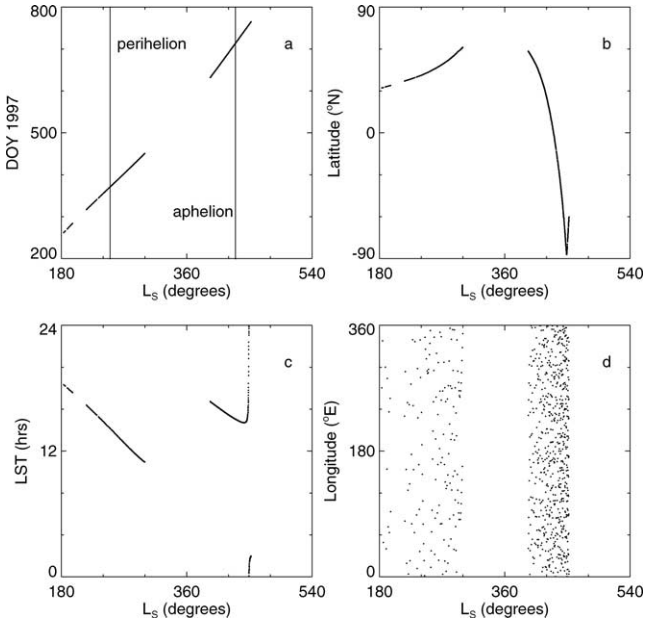

Fig. 1. Parameters of periapsis during aerobraking: (a) periapsis date in days since January 1, 1997 (DOY 1997), (b) periapsis latitude, (c) periapsis LST, and (d) periapsis longitude; all plotted against heliocentric longitude, L_s. Phase 1 of aerobraking occured before $L_s = 360°$ and Phase 2 afterwards. The change from daytime to nighttime LSTs as periapsis reached its furthest south can be seen at $L_s \approx 450°$. The L_s of perihelion and aphelion are marked on panel (a) for reference.

(subset 1) and the "Polar Crossing" (subset 2). The boundary between these two subsets is defined as when a specified point on the aerobraking pass crosses the 60°S boundary on the dayside part of Phase 2. When discussing, for example, data at 130 km altitude from the inbound leg of aerobraking passes, all aerobraking passes in which the latitude at 130 km on the inbound leg is south of 60°S are classified in the Polar Crossing part of Phase 2. For data at different altitudes, or from the other leg of the aerobraking pass, a slightly different group of aerobraking passes forms the Polar Crossing part of Phase 2. As a rough guide, the first periapsis latitude southward of 60°S occurred on orbit 1095. The dayside is defined in this paper as LSTs between 06 and 18 h. The nightside is defined as LSTs between 18 and 06 h. In the polar night, the sun will be below the horizon on both dayside and nightside.

Data from the Accelerometer Experiment is archived in the Planetary Data System (PDS) (Keating et al., 2001a,b). This dataset contains density profiles from 800 aerobraking passes and data extracted from both the inbound and outbound legs of 768 of them at 130, 140, 150, and 160 km altitude. The constant altitude data was used for this work.

3. Sol-to-sol variability

In this section we quantify sol-to-sol variability in the atmosphere to test whether we can meaningfully compare density measurements made at different longitudes on different days as if they were made simultaneously. Such comparisons will be important in the remainder of this paper.

During aerobraking, the orbital period of MGS decreased from over 30 h to less than two hours. Whenever the orbital period was a submultiple of Mars's 24.6 h rotational period, repeated density measurements were made along essentially the same flight paths, that is longitude/altitude/latitude, at one sol intervals. When the rotational period is n times the orbital period, then we say that MGS is in the n:1 resonance. Such a "resonance" typically lasted for several sols as the orbital period decreased through the resonance condition. In the 1:1 resonance, an aerobraking pass traces the same altitude/latitude/longitude path as the one before it. In the 2:1 resonance, there are two different altitude/latitude/longitude paths 180° apart in longitude traced through the atmosphere on each aerobraking pass, each traced by every second one. In the n:1 resonance, paths are $360°/n$ apart, each traced by every nth aerobraking pass. If the outbound legs at, say, 130 km are considered, and the latitudes and longitudes of each orbit in the n:1 resonance are plotted, then they form n clusters separated by $360°/n$ of longitude. We will study the different density measurements taken in these very restricted altitude/latitude/longitude clusters during various resonances. If the atmosphere does not change from one sol to the next, then all the measurements in a given cluster should be the same. Our measure of the sol-to-sol variability is the standard deviation of the density measurements in a cluster, expressed as a percentage of the mean of the density measurements in that cluster. For example, the number "50" implies a standard deviation equal to half of the mean.

Orbits were assigned to the n:1 resonance if their periods were within 3% of the appropriate submultiple of the martian sidereal day. With this criterion, the latitudes and longitudes at, say, 130 km on the inbound leg of each orbit in the resonance formed well-defined clusters (typically 10° wide in longitude and somewhat narrower in latitude) with enough orbits in each cluster to measure a meaningful atmospheric sol-to-sol variability.

Fig. 2 shows the sol-to-sol variability for the 3:1 to 8:1 resonances. These resonances occurred during the Daytime Precession part of Phase 2. Crosses mark the latitude and longitude of each density measurement at a certain altitude whose orbital period satisfies our resonance criterion. Fewer crosses are plotted at higher altitudes because many orbits do not have good density measurements at the higher altitudes. This is especially common in the southern (winter) hemisphere, where observed densities were lower than at corresponding northern (summer) latitudes. Each row of crosses on a panel in Fig. 2 corresponds to a different resonance. The n:1 resonance contains n clusters at equally spaced longitudes. By counting the numbers of clusters at a given latitude in a panel of Fig. 2, n for that resonance can be found. This does not work so well at the higher altitudes where nothing is plotted for some clusters because none of the orbits which belong to those clusters have valid density measurements at those altitudes. On panel (a), data

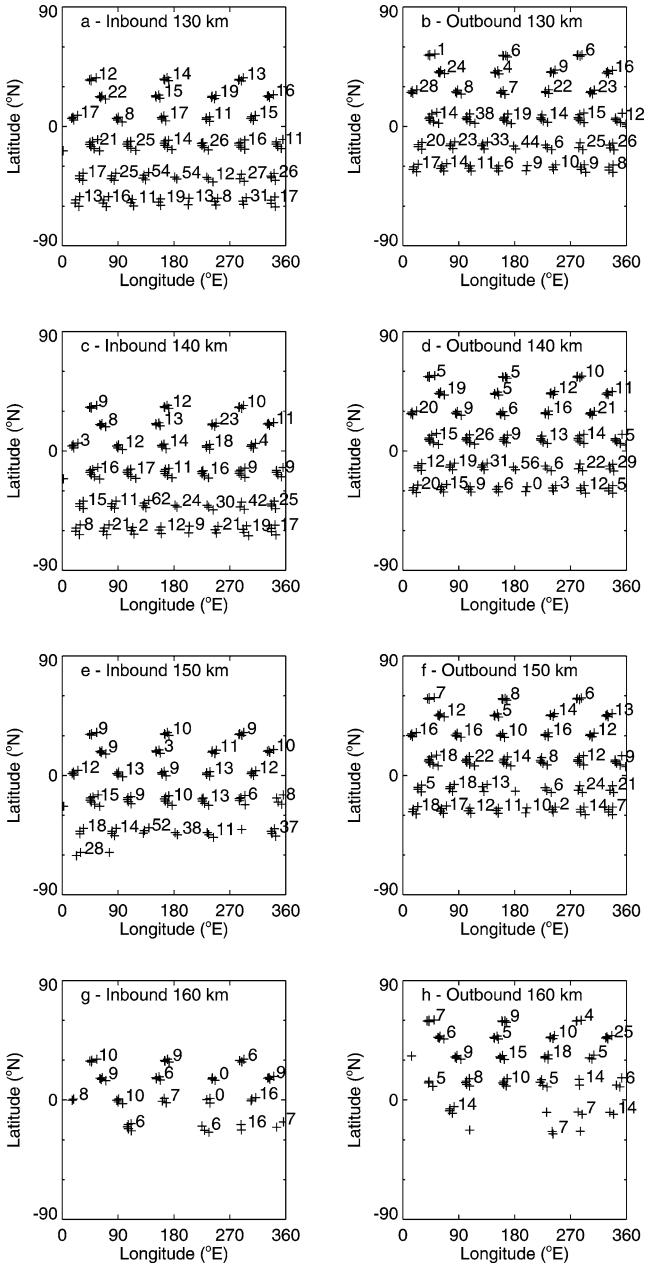

Fig. 2. Latitudes and longitudes of clustered density measurements made at 130, 140, 150, and 160 km altitude on inbound and outbound legs during the 3:1–8:1 resonances, plotted as crosses. The number adjacent to each cluster of crosses is the sol-to-sol variability for that cluster.

in the northernmost three clusters were collected over a few days during the 3:1 resonance. During those same few days of the 3:1 resonance, data in the northernmost three clusters on each panel were collected. A couple of weeks later, data in the second row of four clusters were collected for each panel. On each panel, the same orbits contribute to, say, the northernmost and easternmost cluster. The n:1 resonance at any altitude is further north on outbound than inbound. The latitude of the outbound (inbound) n:1 resonance at a given altitude is further north (south) than at any lower altitude. The numbers adjacent to each cluster are our measure of the sol-to-sol variability in that cluster. Table 1 gives the periapsis latitude, periapsis LST, L_s, and beginning and ending periapsis numbers for each resonance. Periapsis number n was the nth periapsis during the MGS mission.

Table 1
L_s, periapsis latitude, periapsis LST, and beginning and ending periapsis number for the 3:1–8:1 resonances

Resonance	L_s (°)	Latitude (°N)	LST (h)	Beginning periapsis	Ending periapsis
3:1	48	45	16	645	656
4:1	57	32	16	710	725
5:1	64	16	15	784	803
6:1	71	−4	15	864	901
7:1	78	−28	15	963	989
8:1	82	−45	15	1030	1057

1σ measurement errors in the individual density measurements are about 3% or less over 130–150 km, increasing to 5% at 160 km (Keating et al., 2001b). These are negligible compared to the sol-to-sol variability at 130–150 km altitude. At 160 km, the 5% measurement error is smaller than the average sol-to-sol variability of 8–10%, suggesting that we are actually observing sol-to-sol variability and not merely errors in individual measurements. The sol-to-sol variability decreases with increasing altitude. It averages 15–20% at 130 km and 8–10% at 160 km. This is consistent with dissipative processes operating on upwardly propagating disturbances (Zurek et al., 1992; Forbes et al., 2001).

Sol-to-sol variations in density due solely to short-term solar flux variations have been observed in data from Phase 1 of aerobraking (Keating et al., 1998). Keating et al. (1998) observed a 50% increase in density at 160 km altitude at both 32°N and 57°N near orbit 90, with no significant change in density at 130 km altitude, at the same time as an increase in the extreme ultraviolet solar flux incident upon the martian atmosphere. The decrease in sol-to-sol variability with increasing altitude in this section, in contrast to the increase in sol-to-sol variability with increasing altitude in the Keating et al. (1998) example, suggests a mechanism beyond just short-term solar flux variations.

The sol-to-sol variability at the highest northern latitudes is consistently below average. There is a wide variation in sol-to-sol variability over changes in longitude of less than 60°. Neither of these observations can be explained by solar flux variations alone. High sol-to-sol variability might be explained by gravity waves preferentially propagating upwards from certain places when atmospheric conditions are favorable. This is just one possible mechanism, but we do not investigate this any further in this paper.

Preflight estimates of the orbit-to-orbit variability, which includes effects from both sol-to-sol and zonal variabilities, of 35% were realistic (Stewart, 1987; Tolson et al., 1999). The sol-to-sol variability of 15–20% accounts for part of this, with variations in density with longitude accounting for the rest. For comparison, the Earth's day-to-day variability at 200 km altitude can be on the order of 50% during mag-

netic storms, Venus's nighttime density at 150 km can vary by factors of two over 24 h, yet its daytime density varies by less than 10% over the same period (Forbes et al., 1996; Keating et al., 1979; Lyons, 1999).

To answer the question posed at the beginning of this section, it is reasonable to compare density measurements made at different longitudes several days apart as long as differences in density smaller than or similar to the sol-to-sol variability of 15–20% are not automatically attributed to zonal variations.

4. Observations of the zonal structure

4.1. Introduction to the zonal structure

We now move on from studying density measurements at fixed longitude, altitude, latitude, and LST to studying density measurements at varying longitudes and fixed altitude, latitude, and LST. Keating et al. (1998) discovered that large, regular variations in density with longitude exist in the martian upper atmosphere. Similar variations on Earth are significantly smaller (Forbes et al., 1999). Now that we have constrained how much sol-to-sol variability exists, we can examine this zonal structure in density. In this section we discuss our technique for fitting a model to the observed zonal structures.

When MGS's orbital period is not in resonance with the rotational period of Mars, reasonably complete longitudinal coverage is obtained from a small set of consecutive orbits due to the changes in periapsis longitude between each orbit. As periapsis latitude precesses between each orbit, there is a finite range of periapsis latitude in this subset of the data. The same reasoning applies to building up a picture of the zonal structure at a fixed altitude, say 130 km on the outbound legs of aerobraking passes—reasonably complete longitudinal coverage can be obtained over a narrow range in measurement latitude. Fig. 3 shows outbound densities at 130 km altitude between 10°S and 20°S from the Daytime Precession part of Phase 2 of aerobraking. This illustrates the zonal structure. LST (14.7–14.8 h) and L_s (77–80°) are effectively constant for these measurements. Periapsis precessed southward between 10°S and 20°S with large changes in periapsis longitude between each periapsis. The longitudinal sampling is not built up in a regular pattern (e.g., from east to west) and measurements that appear to sample the same longitude repeatedly are not from consecutive orbits. During this period, MGS travelled from south to north on each aerobraking pass with its periapsis between 24°S and 33°S at altitudes of between 108 and 112 km. These data were taken during the 7:1 resonance, a period of significant sol-to-sol variability as can be seen in Fig. 2. Despite the variability in measurements at a given longitude, e.g., 90°E, it is immediately apparent that regular variations in density with longitude exist in the upper atmosphere of

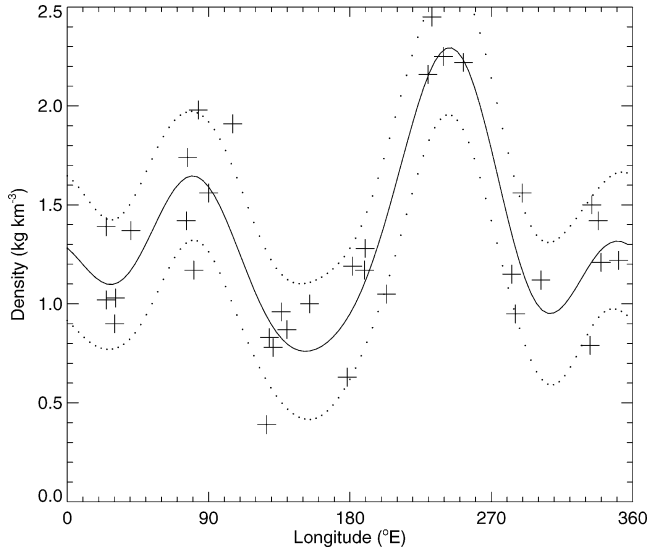

Fig. 3. All outbound density measurements at 130 km altitude between 10°S and 20°S from the Daytime Precession part of Phase 2, crosses, wave-4 harmonic model fit to the data, solid line, and 1σ uncertainties about the fit, dotted lines. The data were collected over about a week, all at an LST of 15 h. Measurement uncertainties (not shown) are much smaller than the range in multiple measurements at any longitude. Zonal structure with large peaks in density at 90°E and 250°E can be seen.

Mars. Density varies by a factor of two over 90° of longitude, greater than the sol-to-sol variability.

Measurement uncertainties are not shown in Fig. 3. As discussed in Section 3, they do not become comparable to the sol-to-sol variabilities until altitudes greater than 150 km. We use a least-squares fit to a harmonic model to characterise the zonal structure. This model contains a constant density term, an amplitude and phase for a sinusoid with one cycle per 360° of longitude, which we label as the wave-1 harmonic, and higher harmonics up to and including wave-4. It has 9 free parameters and we call it a wave-4 model. Measurement uncertainties are not used to constrain the fit. A wave-4 model was chosen because wave-3 models had significantly worse fits to the data in the Daytime Precession part of Phase 2 of aerobraking and wave-5 models did not have significantly better fits. The error envelope plotted on Fig. 3 shows a 1σ uncertainty on what a single new observation at a given longitude might be. We define the phase of a given harmonic as the longitude of its first peak east of 0°. The phase of the wave-n harmonic must lie between 0° and 360°E/n. We generally normalized the zonally-varying terms in each wavefit by their constant density term. This facilitates a comparison of the strength of the zonal structure between different seasons or altitudes.

Throughout this paper, we only attempted model fits to more than 15 data points and only accepted the fit as good if there was a 90% probability that not all model parameters beyond the constant density term should be zero (Neter and Wasserman, 1974). Bad fits generally occurred in regions where there were significantly fewer data points than usual, which might be due either to data dropouts or to a high

rate of periapsis precession through a given latitude range. If fewer than 16 data points were available, then we did not attempt a fit.

4.2. Changes in zonal structure on weekly timescales

As periapsis latitude precessed between orbits, the entire parabolic flight path through the atmosphere shifted with it. This changed the latitude at which MGS passed through, say, 130 km on its outbound leg.

If, as during the Daytime Precession part of Phase 2 of aerobraking, periapsis precesses southward as MGS travels from south to north during each aerobraking pass, then first the 130 km measurement on the inbound leg, and later the same measurement on the outbound leg, will occur at a given latitude.

This gives us two separate opportunities, inbound and outbound, a few weeks apart, to study the atmospheric density at a given latitude, altitude, season, and LST. Season and LST are changing much more slowly than periapsis latitude is precessing. Since periapsis longitude (which is the same as the longitude of the rest of the aerobraking pass away from the polar regions) is continuing to change from one orbit to the next, a picture of the zonal structure at a given latitude range and altitude can be built up on these two separate occasions. In this section we examine how the amplitudes and phases of the harmonics making up the zonal structure change between these two samplings and discuss whether data from the two samplings should be combined or kept separate.

Fig. 3 shows *outbound* densities at 130 km altitude between 10°S and 20°S from the Daytime Precession part of Phase 2 of aerobraking. Fig. 4 shows *inbound* densities at 130 km altitude between 10°S and 20°S from the Daytime Precession part of Phase 2 of aerobraking. The inbound measurements, taken during the 6:1 resonance, were made about two weeks prior to the outbound measurements. The data in each figure were collected over a period of one week. Changes in the zonal structure in this example are minor. Table 2 shows how the amplitudes and phases of the various harmonics change. Only the wave-1 amplitude and wave-2 phase have changed in a statistically significant sense. Recall that the maximum value of the wave-n phase is $360°\mathrm{E}/n$.

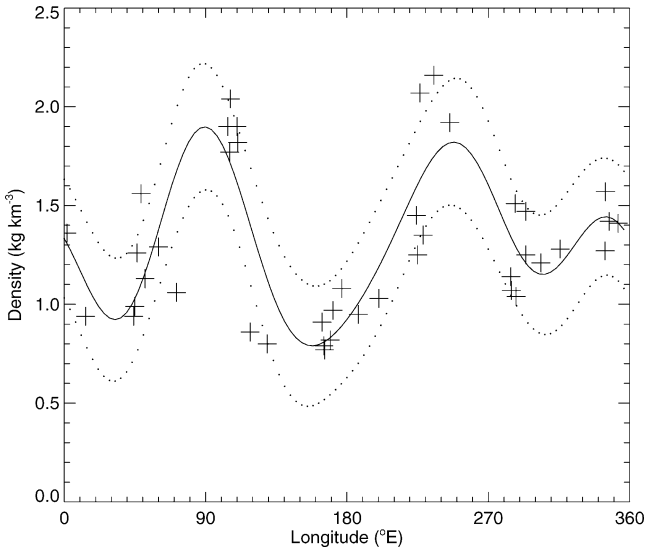

Fig. 4. As Fig. 3, but showing inbound data collected in the same latitude range a couple of weeks earlier. The data were also collected over about a week, all at an LST of 15 h. The amplitudes of the two large peaks have changed somewhat, but their phases have not. The zonal structure is stable on timescales of a couple of weeks.

Table 2
Model fit parameters for measurements made between 10–20°S during the Daytime Precession part of Phase 2. Uncertainties are 1σ

Parameters	Inbound	Outbound
Constant amplitude (kg km^{-3})	1.324 ± 0.042	1.337 ± 0.051
Normalized wave-1 amplitude	0.054 ± 0.045	0.165 ± 0.055
Normalized wave-2 amplitude	0.249 ± 0.058	0.345 ± 0.055
Normalized wave-3 amplitude	0.204 ± 0.059	0.177 ± 0.071
Normalized wave-4 amplitude	0.105 ± 0.058	0.109 ± 0.065
Wave-1 phase (°)	298.7 ± 47.7	260.5 ± 18.3
Wave-2 phase (°)	80.4 ± 6.4	64.1 ± 4.5
Wave-3 phase (°)	103.0 ± 5.1	109.6 ± 7.2
Wave-4 phase (°)	81.5 ± 7.7	74.0 ± 9.7

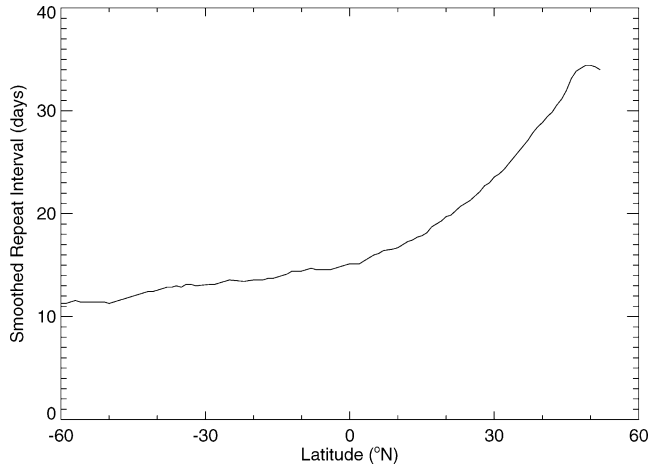

Fig. 5. Interval between inbound measurements at 130 km altitude at a given latitude and later outbound measurements at the same latitude and altitude from the Daytime Precession part of Phase 2.

Fig. 5 shows the interval between repeated density measurements at 130 km altitude as a function of latitude for the Daytime Precession part of Phase 2. Fig. 1 shows that changes in LST and L_s are small on these timescales. This allows us to characterise the zonal structure at a given altitude, latitude, LST, and L_s twice—with an interval on the order of several weeks between the two characterisations.

This leaves us with two options: we may either combine inbound and outbound measurements to characterise a given altitude, latitude, LST, and L_s once only or treat these two halves separately. Combining measurements gives more data points but introduces the issue of having half the data collected over a week, a week of no data, then a week of collecting the last half of the data. Wilson (2002) notes that

the meridional variation of zonal mean density is the same for inbound and outbound, further notes that there is little difference between the zonal structure observed in inbound and outbound data, and then uses inbound and outbound data together. Until we have carefully investigated the statistical similarity of the inbound and outbound wavefits at a given altitude, latitude, LST, and L_s we keep inbound and outbound measurements separate. Each data collection period is thus continuous.

4.3. Changes in zonal structure with altitude

In this section we characterise how the amplitudes and phases of each harmonic in the zonal structure change as a function of altitude and see if this behaviour is affected by latitude.

Density measurements are made at every altitude on each leg of an aerobraking pass. Densities at one altitude can be compared with those at another altitude from the same leg. However, since the two densities are also measured at different latitudes, the comparison does not isolate changes due to altitude alone. Due to the precession of periapsis and with it the entire parabolic flight path through the atmosphere, a density measurement at one altitude and latitude on the outbound leg of an aerobraking pass can be compared to another density measurement at a different altitude, but the same latitude, from the outbound leg of a subsequent aerobraking pass. The precession of periapsis enables us to separate variations due to altitude and latitude despite having non-vertical aerobraking passes. Fig. 3 shows outbound densities at 130 km altitude between 10°S and 20°S. Orbits whose data are shown in Fig. 3 also measured outbound densities at 140 km, but between 9°S and 18°S. Examining all 140 km outbound data between 10°S and 20°S requires a slightly different set of orbits, and so on for other altitude levels.

Fig. 6 shows the zonal structure between 10°N and 20°N on the outbound leg during Phase 2 at 130, 140, 150, and 160 km. These data were taken between the 5:1 and 6:1 resonances. We have shifted from 10–20°S to 10–20°N to show the clearest example. The constant density term decreases monotonically as altitude increases, as expected for the background density structure in any atmosphere, and the zonal structure tends to a zonal mean as altitude increases. All the statistically significant peaks and troughs appear fixed in longitude. The trough at 270°E and peak at 330°E are no longer statistically significant at 160 km altitude.

We have repeated this for other latitude bands between 60°S and 60°N using data from the Daytime Precession part of Phase 2. We generally find that the normalized wave-1 amplitude decreases by about 50% from 130 km to 150 km and those for waves-2, 3, and 4 decrease by about 30%. The rate of change of normalized harmonic amplitude with altitude is influenced by the nature of the atmospheric phenomenon that we observe as zonal structure and will be discussed further in Section 5.1. Wave-1 normalized amplitudes are small and not very statistically significant at higher altitudes. The phase is meaningless when the amplitude is not significant, which is why its formal value changes erratically with increasing altitude. The waves-2, 3, and 4 phases can change by up to 10–20° with increasing altitude, but are not systematic in an eastward or westward sense within any restricted latitude region and are most consistent with no change in phase with increasing altitude.

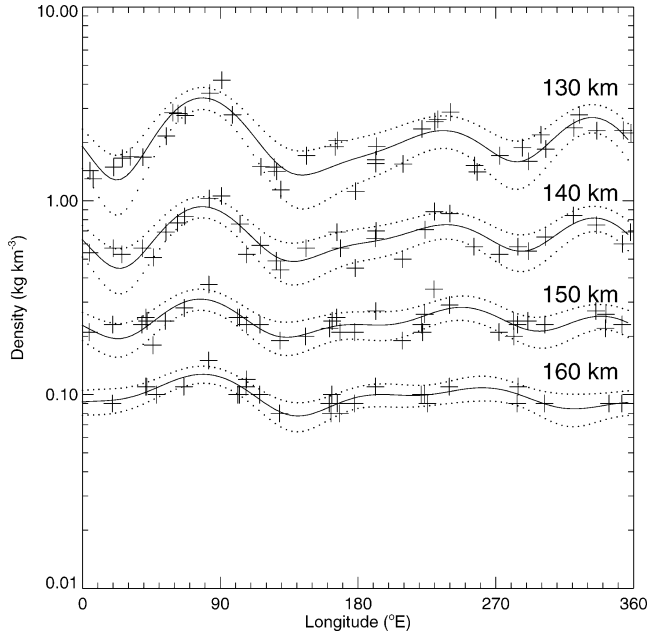

Fig. 6. Density measurements at 130, 140, 150, and 160 km altitude between 10°N and 20°N for outbound measurements during the Daytime Precession part of Phase 2, plotted as crosses. Model fits to data from each altitude are plotted as solid lines and 1σ uncertainties about each fit as dotted lines. Measurement uncertainties (not shown) are much smaller than the range in multiple measurements at any altitude and longitude. All data were taken at an LST of 15 h. Measurements at each altitude level were taken over about a week, but this interval is offset by a couple of days between one altitude level and the next. All density measurements are associated with the obvious altitude level; there are no pathological cases of, say, a 140 km density measurement lurking within the range of the 130 km measurements.

Decreases in normalized harmonic amplitude as altitude increases are evidence of dissipation. Classical tidal theory, which assumes a dissipationless medium, predicts that these normalized amplitudes should increase as altitude increases (Chapman and Lindzen, 1970). Possible causes of this dissipation include radiative cooling, wave–wave coupling, shear instabilities, and viscosity (Hooke, 1977; Forbes, 1995).

4.4. Changes in zonal structure with latitude

In this section we examine changes in the normalized amplitudes and phases of each harmonic in the zonal structure as a function of latitude, discuss whether the zonal structure is planetary-scale or localised, and quantify which harmonics are dominant.

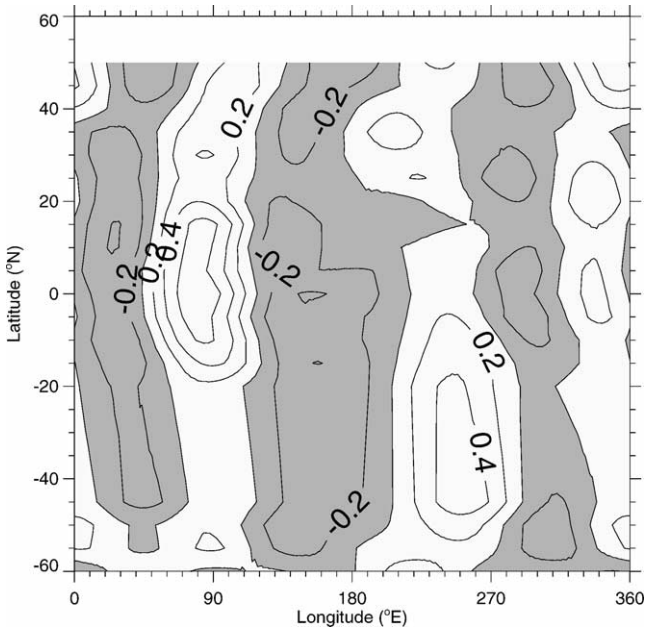

Fig. 7. Contour plot of normalized fitted densities at 130 km altitude, inbound leg, from the Daytime Precession part of Phase 2. The normalization highlights the zonal structure. The LST of the data is 17 h in the north, decreasing to 15 h in the south. The L_s of the data is 30° in the north, increasing to 80° in the south. Contour intervals are 0.2 (dimensionless) and negative regions (low densities) are shaded. The peaks and troughs from Fig. 4 can be seen between 10°S and 20°S.

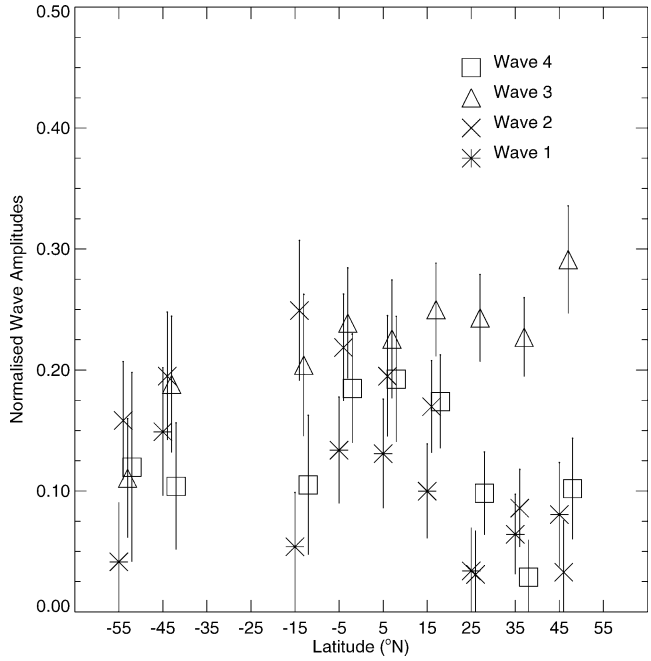

Fig. 8. Normalized amplitudes from the wave-4 harmonic fits that were merged to create Fig. 7. The latitude of each set of harmonics is the centre of the 10° wide latitude band from which all the density measurements that contributed to the harmonic fit came. Only every other fit used in Fig. 7 is shown; including every fit increases the clutter without aiding interpretation. Gaps at 25°S and 35°S are due to bad fits which were not included in Fig. 7.

In Section 4.1, we built up a picture of the zonal structure at 130 km using outbound data. In order to sample enough longitudes we had to include data from so many orbits that the measurement latitude precessed from 10°S at the first density measurement to 20°S at the last density measurement. By allowing periapsis latitude (and the latitude corresponding to the measurement altitude) to precess still further, we can see how the zonal structure changes from one latitude range to another.

Fig. 7 shows the zonal structure as a function of latitude for inbound data at 130 km altitude from the Daytime Precession part of Phase 2. Wavefits similar to Fig. 4 were constructed at five degree intervals with ten degree windows in latitude, normalized by their constant density term, then merged into a contour plot. There is overlap between adjacent latitude windows, so adjacent wavefits are not statistically independent. The overlap is included to smooth the contours. Fig. 7 should be compared to Fig. 1 of Wilson (2002) which uses both inbound and outbound data. The two figures are similar, as they should be according to Section 4.2. Only wavefits from latitude ranges which yielded a good fit, as discussed in Section 4.1, are included in this plot. Latitude ranges with bad fits, 20–40°S, include orbits 911–961 which have poor or missing data due to spacecraft computer problems. Since zonal fits in this range are poor because of inadequate data, this region in Fig. 7 is filled by the interpolation of nearby fits. Uncertainties in the fitted density as a function of latitude and longitude are not shown, but the mean 1σ uncertainty is 20% of the constant density term with most values within a few percentage points of this mean. Fig. 4 shows the uncertainty in the fit in one latitude range.

A contour plot similar to Fig. 7, but using outbound data, can also be constructed. Measurements at a given altitude and latitude are taken first on the inbound leg and then, a few weeks later, on the outbound leg. A contour plot similar to Fig. 7, but at a different altitude, can also be constructed. There is also a few days difference in time between measurements at a given latitude and different altitudes. All these similar contour plots have a high density peak at 80°E, most prominent in the northern hemisphere, a high density peak at 250°E, most prominent in the southern hemisphere, and a high density peak at 330°E. The peak at 330°E is always the smallest and the other two peaks are relatively large.

The meridionally broad nature of the zonal structure is immediately apparent. Together with its stability on fortnightly timescales, discussed in Section 4.2, and its consistent behaviour with altitude at different latitudes, discussed in Section 4.3, this implies that whatever atmospheric phenomenon is causing the zonal structure operates on a planetary scale. At first glance, given the two large peaks 180° apart, the wave-2 harmonic appears dominant.

Figs. 8 and 9 show the normalized amplitudes and phases of the harmonic fit displayed in Fig. 7 over a range of latitudes. The situation is more complicated than a mere wave-2 dominance. Wave-3 is dominant in the northern extratropics and no single harmonic is dominant in the southern ex-

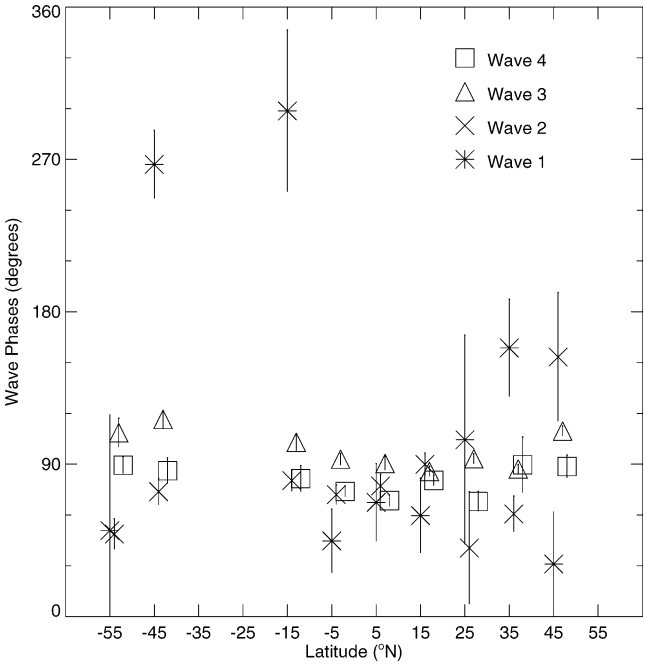

Fig. 9. Phases corresponding to the amplitudes in Fig. 8. Recall that the maximum value of the phase of the wave-n harmonic is 360°E/n.

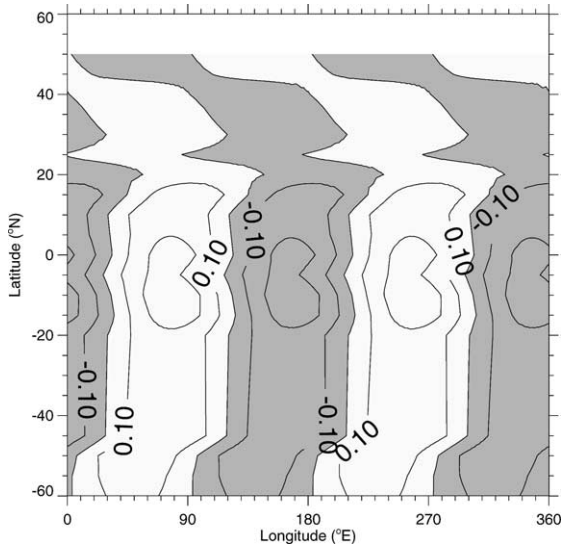

Fig. 10. As Fig. 7, but plotting only the wave-2 components. Contour intervals are 0.1 and negative regions (low densities) are shaded.

tratropics or the tropics. Wave-1 is the weakest harmonic over the entire range of latitude. Waves-2, 3, and 4 all have phases, all around 90°E, which stay remarkably constant over a wide range of latitude. This constancy is additional evidence that a planetary-scale mechanism is responsible for the zonal structure. Similar conclusions are reached from the study of outbound data and/or different altitudes.

Figs. 10 and 11 show the wave-2 and wave-3 components of Fig. 7. They should be compared to Figs. 2a and 2b of Wilson (2002). The two pairs of figures are similar, as they should be according to Section 4.2. The constancy of the

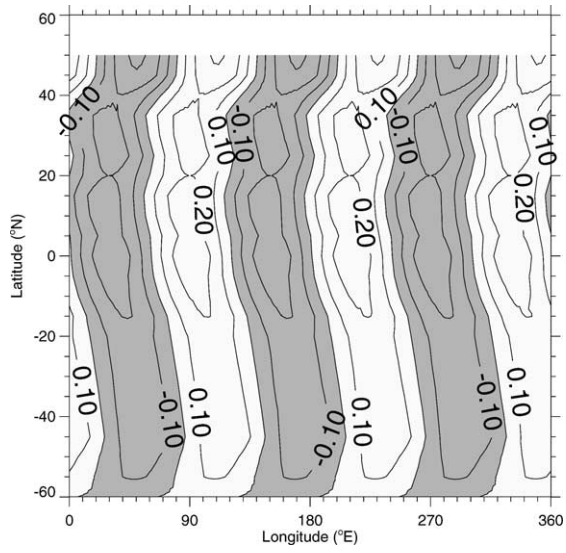

Fig. 11. As Fig. 7, but plotting only the wave-3 components. Contour intervals are 0.1 and negative regions (low densities) are shaded.

phases can be seen, as can the way in which these two harmonics interfere to yield the apparent wave-2 dominance in Fig. 7. Overlaps between peaks in the wave-2 and wave-3 harmonics (i.e., constructive interference to give large densities) occur at about 80°E (mainly in the northern hemisphere) and 250°E (mainly in the southern hemisphere). The wave-3 peak at 330°E destructively interferes with the wave-2 trough at the same longitude to give only a small peak in density. The shift in the phase of the wave-3 harmonic with latitude is responsible for the shift of the largest peak in the zonal structure from 80°E in the northern hemisphere to 250°E in the southern hemisphere.

Fig. 8 shows erratic changes in normalized harmonic amplitude with latitude, in contrast to the well-behaved phases of Fig. 9. This may represent the individual responses by each tidal mode to whatever surface inhomogeneity is causing the zonal structure and/or the ease of propagation through the lower atmosphere at this latitude. Insight into this behaviour may come from new surface-to-thermosphere GCMs currently under development (Bougher et al., 2002; Angelats i Coll et al., 2002).

The total energy associated with each harmonic in a given latitude band is proportional to the product of the area of the latitude band and the square of the amplitude. A measure of the global strength of each harmonic is its root-mean-square (rms) normalized amplitude, where the mean-square normalized amplitude has been weighted by the cosine of latitude. Using both inbound and outbound harmonic amplitudes at 130 km altitude, we find that the wave-3 rms normalized amplitude of 22% is greatest. Wave-2 is the next strongest at 18%, followed by wave-4 at 14% and wave-1 at 12%. The 1σ uncertainties in the rms normalized amplitudes are 1%. Wave-2 is not the most important harmonic in the observed zonal density structures; wave-3 is.

Wilson (2002) used a GCM to model atmospheric densities at 130 km altitude and below. He found wave-2 and wave-3 to be the strongest harmonics at 120 km altitude, with wave-2 stronger than wave-3, and reproduced the lack of phase variation with changes in latitude.

4.5. Changes in zonal structure with local solar time

In this section we use data from the Polar Crossing part of Phase 2 of aerobraking to examine the week-to-week repeatability of the zonal structure in polar regions, then compare the normalized amplitudes and phases of harmonics in dayside and nightside zonal structures in polar regions.

During the Daytime Precession part of Phase 2, periapsis latitude precessed southward with little change in periapsis LST from one orbit to the next, little change in longitude from atmospheric entry to exit during an individual aerobraking pass, and little change in LST from atmospheric entry to exit during an individual aerobraking pass. This is shown in Fig. 1. Periapsis cannot continue to precess southward indefinitely. As periapsis continued to precess around in the orbital plane, it reached an extreme southern latitude, then precessed northward. Periapsis, which was on the sunward, daytime side of Mars, has shifted to the antisunward, nighttime side of Mars. The extreme southern latitude ($\sim 87°$S) is set by the inclination of MGS's orbital plane. Since periapsis crossed the terminator during this Polar Crossing, periapsis LST must change from one orbit to the next.

As in the Daytime Precession part of Phase 2, periapsis longitude changes from one orbit to the next during this Polar Crossing. Unlike the Daytime Precession behaviour, the longitude of MGS during an individual aerobraking pass also changes during this Polar Crossing. The longitude of MGS must steadily track through all 360° during one orbit. At polar latitudes, MGS's longitude will change significantly over short arcs of an orbit as MGS crosses the converging lines of longitude. When periapsis occurs close to the pole, MGS's longitude will change significantly over the short arc that is the aerobraking pass. MGS's LST will change significantly during an individual aerobraking pass for exactly the same reason.

As periapsis precesses southwards towards the pole, the 130 km altitude level on the inbound leg occurs to the south of periapsis and periapasis occurs to the south of the 130 km level on the outbound leg. That is, MGS travelled from south to north during an aerobraking pass before reaching its furthest south. The 130 km altitude level on the inbound leg reaches its furthest south, crosses the terminator from day to night, and moves northward before periapsis does. Periapsis, in turn, does so before the 130 km altitude level on the inbound leg. When periapsis was at its furthest south, MGS travelled from north to south on the inbound leg, then from south to north on the outbound leg.

When periapsis is exactly at its furthest south, the latitudes at which the inbound and outbound legs cross, say, the 130 km altitude level are the same. This is a consequence of the reflection symmetry of an ellipse (such as an orbit) about its semimajor axis. With a near-polar orbit, the LSTs of these two points are about half a sol apart. Density measurements can be made a few minutes apart at exactly the same latitude and altitude, half a sol apart in LST. By considering several orbits close to when periapsis was at its furthest south, a picture of the daytime and nighttime zonal structure at a given altitude and this altitude can be built up.

In practice, enough data to build up a picture of the zonal structure at, say, 130 km takes so many orbits to acquire that there is a finite range in the latitude of the measurements (as in Section 4.1). We use a 20° wide latitude range, instead of the usual 10°, because there are fewer measurements per degree of latitude at this stage of aerobraking than before.

When periapsis is at its furthest south, the inbound and outbound legs cross the 130 km altitude level at about 70°S. At this time, the 130 km altitude level on the inbound leg is moving north, the same altitude level on the outbound leg is moving south. To build up a picture of the zonal structure at 130 km between 50°S and 70°S, we must use data from the preceding week for the outbound case and data from the following week for the inbound case. Despite this difference of about a week between the two sets of observations at 50–70°S, can we compare them as if they were taken simultaneously? We addressed this problem for non-polar regions in Section 4.2 and found that we could do so. Here we should examine the week-to-week repeatability of both the daytime and the nighttime zonal structure. We would like to compare daytime measurements at 130 km between 50°S and 70°S for inbound and outbound legs. We would also like to compare nighttime measurements at 130 km between 50°S and 70°S for inbound and outbound legs. However, aerobraking ended when the 130 km altitude level on the outbound leg reached its furthest south and repeat nighttime measurements are not available.

There are three relevant subsets of data at 130 km altitude between 50°S and 70°S; inbound on the dayside with MGS travelling from south to north through the atmosphere, outbound on the dayside with MGS travelling from south to north through the atmosphere, and inbound on the nightside with MGS travelling from north to south through the atmosphere. Due to the cold temperatures and consequently decreased densities, nightside data at higher altitudes is not available in useful quantities. Fig. 12 shows the intervals between these three sets of measurements at a given latitude. In the 50–70°S latitude band, the 11 day interval between inbound dayside and outbound dayside measurements is longer than the interval between inbound nightside and outbound dayside measurements. The difference in LST between the nightside measurements at LST = 02 h and the dayside measurements at LST = 15 h is very close to half a sol. Figs. 13–15 show wavefits for the three sets of measurements at 130 km altitude between 50°S and 70°S. Each of the three includes a couple of resonances, the 8:1 and

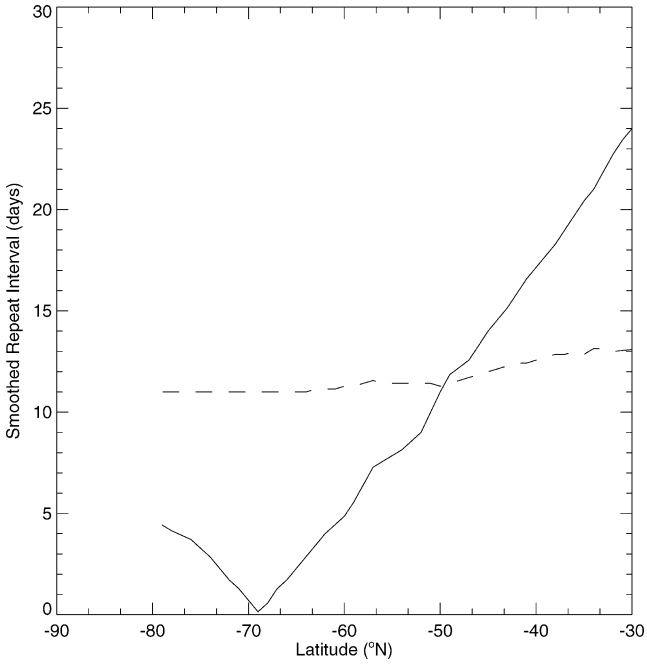

Fig. 12. Interval between outbound dayside measurements at 130 km altitude and a given latitude and inbound nightside measurements at the same latitude and altitude (solid line) from Phase 2. The minimum near 70°S occurs when periapsis is at its furthest south. At more northern latitudes, outbound dayside measurements preceed inbound nightside measurements. At more southern latitudes, inbound nightside measurements preceed outbound dayside measurements. Also plotted is the interval between outbound dayside measurements at 130 km altitude and a given latitude and inbound dayside measurements at the same latitude and altitude (dashed line) from Phase 2. Inbound dayside measurements always preceed outbound dayside measurements. South of 50°S, the interval between day–night repeat measurements at a given latitude and 130 km altitude is less than that between day–day repeat measurements at that latitude and altitude.

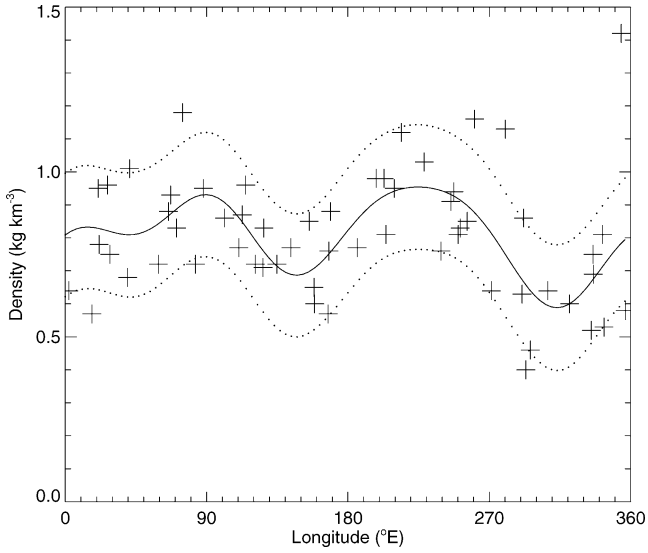

Fig. 13. All inbound dayside density measurements at 130 km altitude between 50°S and 70°S from Phase 2, crosses, wave-4 harmonic model fit to the data, solid line, and 1σ uncertainties about the fit, dotted lines. The data were collected over about a week, all at an LST of 15 h. Measurement uncertainties (not shown) are much smaller than the range in multiple measurements at any longitude. The zonal structure is less pronounced that in Fig. 3 or others from the tropics, but is still significant above a zonal mean.

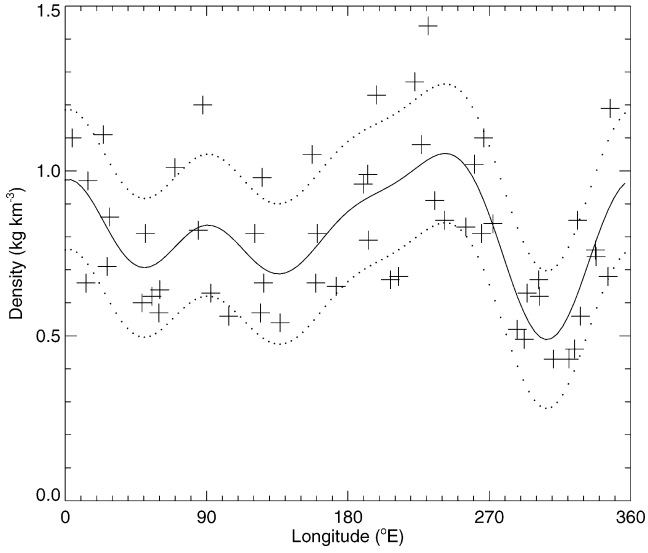

Fig. 14. As Fig. 13, but using outbound dayside density measurements. The data used here were collected about 11 days after those in Fig. 13, but the weak zonal structure is still broadly the same.

9:1 for inbound on the dayside, the 10:1 and 11:1 for outbound on the dayside, and the 11:1 and 12:1 for inbound on the nightside. The normalized amplitudes and phases of the various harmonics are shown in Table 3. A comparison between the inbound dayside and outbound dayside results is consistent with the results of Section 4.2 for more equatorial latitudes—changes in normalized amplitudes and phases are minor.

Assuming that the nightside atmosphere does not change more rapidly than the dayside atmosphere does, we can compare the phases of the inbound nightside and outbound dayside wavefits as if the measurements were effectively simultaneous. There is no way to test this assumption with the MGS accelerometer data. The formal amplitude of each of the four harmonics has increased from day to night, but with little statistical significance. The phase of the wave-1 harmonic changes by approximately 90°, the phase of the wave-2 harmonic changes by approximately 90°, and the phase of the wave-3 harmonic does not change significantly. The wave-4 harmonic is not statistically significant in the nightside wavefit. These phase changes have implications for the nature of the atmospheric phenomenon that we observe as zonal structure and will be discussed further in Section 5.1.

Bougher et al. (2001) found evidence for a zero phase shift in a wave-3 zonal density harmonic at 64–67°N between 04 and 16 h LST in their comparisons of electron and neutral density, but did not present a detailed harmonic breakdown.

Table 3
Model fit parameters for measurements made at 130 km between 50–70°S during Phase 2. Uncertainties are 1σ

Parameters	Inbound dayside	Outbound dayside	Inbound nightside
Constant amplitude (kg km^{-3})	0.807 ± 0.023	0.810 ± 0.027	0.383 ± 0.033
Normalized wave-1 amplitude	0.069 ± 0.040	0.083 ± 0.047	0.275 ± 0.125
Normalized wave-2 amplitude	0.148 ± 0.041	0.168 ± 0.046	0.280 ± 0.115
Normalized wave-3 amplitude	0.066 ± 0.040	0.134 ± 0.046	0.202 ± 0.118
Normalized wave-4 amplitude	0.051 ± 0.049	0.101 ± 0.048	0.126 ± 0.139
Wave-1 phase (°)	154.8 ± 33.0	207.1 ± 32.2	107.7 ± 24.2
Wave-2 phase (°)	52.4 ± 7.6	37.1 ± 8.2	117.0 ± 12.4
Wave-3 phase (°)	108.3 ± 11.5	117.3 ± 6.7	114.8 ± 10.8
Wave-4 phase (°)	3.4 ± 10.2	85.4 ± 6.4	88.9 ± 11.4

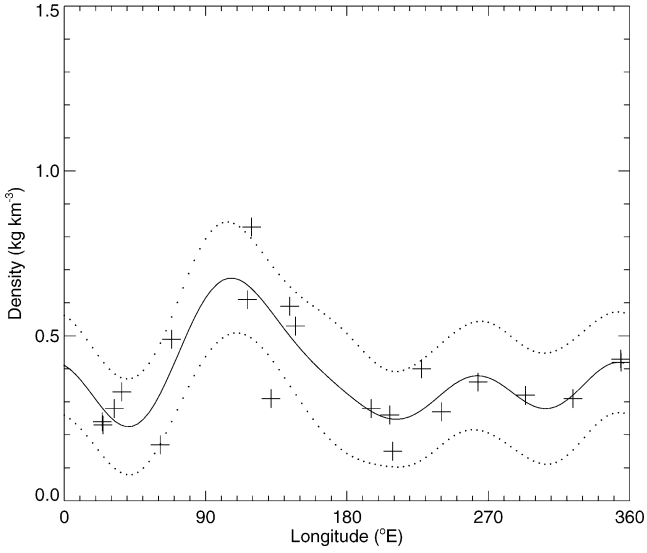

Fig. 15. As Fig. 13, but using inbound nightside density measurements. The LST is 02 h. Densities have decreased from day to night, and the zonal structure is very different.

5. Modeling of the zonal structure

5.1. Constraints on tidal modes responsible for zonal structure

The zonal structures observed in the martian upper atmosphere can be studied using tidal theory. "Atmospheric tides are global-scale oscillations in temperature, wind, density, and pressure at periods which are subharmonics of a solar or lunar day" (Forbes, 1995). The dominant forcing in the martian atmosphere is solar heating. Tidal variations in density at fixed altitude, latitude and season with dependence on longitude and LST can be represented as (Chapman and Lindzen, 1970; Forbes and Hagan, 2000; Wilson, 2000)

$$\rho(\lambda, t_{\mathrm{LST}}; z, \theta, L_s) = \sum_{\sigma,s} \rho_{\sigma,s}(z, \theta, L_s) \cos\big(\sigma\Omega(t_{\mathrm{LST}} - \lambda/2\pi) + s\lambda - \phi_{\sigma,s}(z, \theta, L_s)\big), \quad (1)$$

where ρ is density, λ is east longitude, t_{LST} is local solar time in sols, z is altitude, θ is latitude, L_s is heliocentric longitude or season, σ is the temporal harmonic ($\sigma = 0, 1, 2, \ldots$), s is the zonal wavenumber ($s = \ldots, -2, -1, 0, 1, 2, \ldots$), $\Omega = 2\pi$ sol^{-1}, and $\phi_{\sigma,s}$ is the phase.

Westward propagating tides have $s > 0$, eastward propagating tides have $s < 0$, and zonally-symmetric tides have $s = 0$. Migrating tides, which have $s = \sigma$, have zonal phase speeds equal to that of the Sun as seen by a fixed observer (Forbes and Hagan, 2000). Non-migrating tides have $s \neq \sigma$. Only migrating tides are excited in a zonally-symmetric atmosphere with zonally-symmetric boundary conditions. If asymmetries are present in the atmospheric boundary conditions, such as albedo, thermal inertia, or topography, then their interactions with the migrating tides generate non-migrating tides (Forbes et al., 1995; Forbes and Hagan, 2000). Zonal inhomogeneities distributed throughout the lower atmosphere, such as dust loading, can also generate non-migrating tides. The non-migrating tides excited by asymmetries of the form $\cos(m\lambda - \phi_m)$, where m is the zonal wavenumber of the asymmetry, are (Forbes and Hagan, 2000)

$$\rho(\lambda, t_{\mathrm{LST}}; z, \theta, L_s) = \sum_{\sigma,m} \rho_{\sigma,m}(z, \theta, L_s) \cos\big(\sigma\Omega t_{\mathrm{LST}} \pm m\lambda - (\phi_\sigma(z, \theta, L_s) \pm \phi_m)\big). \quad (2)$$

Solar heating is well described by a combination of diurnal ($\sigma = 1$) and semidiurnal ($\sigma = 2$) harmonics. When the migrating diurnal and semidiurnal tides interact with an $m = 1$ asymmetry, such as topography, they are modulated to form the $s = 0$ and $s = 2$ diurnal tides and the $s = 1$ and $s = 3$ semidiurnal tides respectively (Forbes and Hagan, 2000). All four of these non-migrating tidal modes appear as zonal variations with wavenumber 1 as seen from the fixed LST reference frame of MGS. Each of the zonal harmonics identified in the accelerometer dataset at fixed LST is influenced by a near-surface asymmetry with the same zonal wavenumber and could be attributable to four possible tidal modes. When we observe a harmonic in the accelerometer dataset, which of the four possible tidal modes is responsible?

In the classical tidal theory of a highly idealized atmosphere, each σ, s tidal mode can be decomposed into a complete, orthogonal set of functions, called Hough modes,

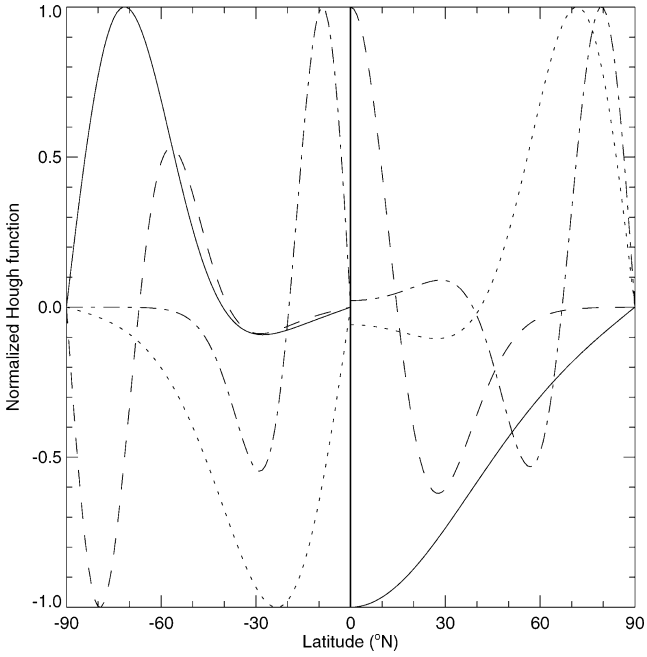

Fig. 16. Meridional structure of the eight lowest order Hough modes with $\sigma = 1$, $s = -1$. Asymmetric functions are shown in the southern hemisphere only, symmetric functions are shown in the northern hemisphere only. Asymmetric functions are $n = -1$ (solid line), $n = 2$ (dotted line), $n = -3$ (dashed line), $n = 4$ (dot-dash line). Symmetric functions are $n = 1$ (solid line), $n = -2$ (dotted line), $n = 3$ (dashed line), $n = -4$ (dot–dash line).

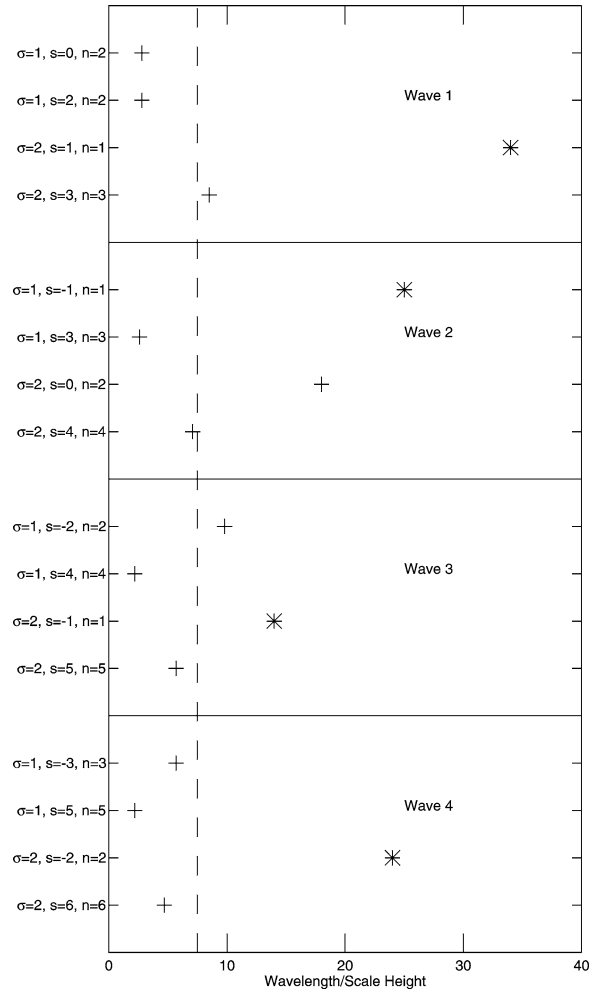

Fig. 17. Vertical wavelengths of the 16 σ, s, n Hough modes that satisfy the excitation criteria. Travelling waves are marked with a cross and evanescent waves are marked with an asterisk. The dashed line represents the propagation criterion—Hough modes with vertical wavelengths greater than 7.5 scale heights can propagate to the upper atmosphere.

that are each labeled with an index n (Chapman and Lindzen, 1970). The meridional structure of each σ, s, n Hough mode is separable from its vertical structure. Note that we refer to a disturbance with a given temporal and zonal structure as a σ, s tidal mode and to one with a given temporal, zonal, meridional, and vertical structure as a specific σ, s, n Hough mode.

Roughly speaking, the meridional structure of a specific σ, s, n Hough mode determines whether it will be efficiently excited by solar heating and its vertical structure determines whether it will be able to propagate to the upper atmosphere. If none of the σ, s, n Hough modes that make up a given σ, s tidal mode can be efficiently excited by solar heating *and* propagate to the upper atmosphere, then that σ, s tidal mode cannot influence the accelerometer measurements of the zonal structure.

For a σ, s, n Hough mode to contribute strongly to the zonal structure in the upper atmosphere, it must be efficiently excited by solar heating. Like solar heating, it must be symmetric about the equator, be peaked at the equator rather than poleward of the tropics, and have no nodes (latitudes at which its amplitude is zero) too close to the equator. Fig. 16 shows 8 Hough modes with $\sigma = 1$, $s = -1$. The observed wave-2 zonal structure could be attributable to any of these 8 Hough modes. n ranges from 1 to 4 and from -1 to -4. Only the $n = 1$ mode comes close to satisfying the above excitation criteria. It is the first (i.e., lowest absolute value of n) symmetric mode for this σ, s combination. For each of the 16 σ, s diurnal and semidiurnal tidal modes that could be influencing the wave-1 to wave-4 harmonics in the accelerometer dataset, only the first symmetric σ, s, n Hough mode satisfied the excitation criteria. The first symmetric, diurnal, and eastward propagating Hough mode for a given zonal wavenumber $-s$ is called a diurnal Kelvin wave and labeled as DKs. The $\sigma = 1$, $s = -1$, $n = 1$ mode that satisfies the excitation criteria above is DK1.

In the idealized case of classical tidal theory, a Hough mode propagates vertically as either an evanescent or a travelling wave (Chapman and Lindzen, 1970). In reality, damping in the martian atmosphere is quite strong for even the travelling waves (Zurek et al., 1992; Forbes et al., 2001). Fig. 17 shows the vertical wavelengths of the 16 σ, s, n Hough modes that satisfied the above excitation criteria. An altitude of 130 km, representative of the accelerometer dataset, corresponds to about 15 scale heights above the martian surface. We assert that, of the Hough modes in Fig. 17, the travelling Hough modes with vertical wave-

Table 4
Hough modes satisfying the excitation and propagation criteria

Hough mode	Zonal wavenumber at fixed LST	Wavelength in scale heights
$\sigma = 2,\ s = 1,\ n = 1$	1	34 (Evanescent)
$\sigma = 2,\ s = 3,\ n = 3$	1	8.5
$\sigma = 1,\ s = -1,\ n = 1$ (DK1)	2	25 (Evanescent)
$\sigma = 2,\ s = 0,\ n = 2$	2	18
$\sigma = 1,\ s = -2,\ n = 2$ (DK2)	3	9.8
$\sigma = 2,\ s = -1,\ n = 1$	3	14 (Evanescent)
$\sigma = 2,\ s = -2,\ n = 2$	4	24 (Evanescent)

lengths greater than 7.5 scale heights (those which undergo no more than two complete cycles before reaching 130 km altitude) and all the evanescent Hough modes (whose smallest vertical wavelength is 14 scale heights) can propagate to the upper atmosphere. This propagation criterion suggests that only the σ, s, n Hough modes listed in Table 4 are plausibly contributing to the zonal structure. In cases where more than one Hough mode could be contributing to a given zonal density harmonic, both could be operating simultaneously. The relatively rapid decrease in the normalized amplitude of the wave-1 harmonic with altitude, discussed in Section 4.3, suggests that its Hough mode has a shorter vertical wavelength than those causing the other zonal harmonics. This favours the $\sigma = 2$, $s = 3$, $n = 3$ Hough mode over the $\sigma = 2$, $s = 1$, $n = 1$ Hough mode in Table 4.

Observations at widely spaced LSTs can be used to reject some of the possible Hough modes in Table 4. Diurnal and semidiurnal Hough modes, if contributing to the zonal structure, will cause different changes in the phase of harmonics in the zonal structure over intervals of half a sol. The results of Section 4.5 (Table 3) lead us to conclude that the wave-1 zonal density harmonic is not associated with one of the two possible Hough modes in Table 4, the wave-2 zonal density harmonic is attributable to the $\sigma = 1$, $s = -1$, $n = 1$ Hough mode (DK1), the wave-3 zonal density harmonic to the $\sigma = 2$, $s = -1$, $n = 1$ Hough mode, and the wave-4 zonal density harmonic, where present, to the $\sigma = 2$, $s = -2$, $n = 2$ Hough mode. The wave-1 zonal density harmonic shows a phase change of about 90°, midway between the 0° change of a semidiurnal harmonic and the 180° change of a diurnal harmonic, so it cannot be explained by this simplified model. These preliminary conclusions are independent of any previous modeling or observational work, have neglected the effects of winds, and are reexamined at the end of Section 5.2.

5.2. Other tidal observations and theory

In this section we discuss previous modeling and observational work on tides in the martian atmosphere that is relevant to Section 5.1 and then reexamine that section's preliminary conclusions in light of the additional information.

Bougher et al. (2001) identified the $\sigma = 2$, $s = -1$ tidal mode as the most likely cause of the wave-3 harmonic they observed in both neutral density data and electron density data at 64–67°N latitude and $L_s = 70°$.

Joshi et al. (2000) used the results of Hollingsworth and Barnes (1996) to argue against the hypothesis of Keating et al. (1998) that stationary waves were responsible for the zonal structure observed during Phase 1 of aerobraking. They also suggested that the observed zonal structure could be due to diurnally varying tidal modes. Simulations at 80 km altitude gave reasonable agreement with the observed phasing of the peaks.

Forbes and Hagan (2000) investigated the $\sigma = 1$, $s = -1$, $n = 1$ Hough mode (DK1). For simulated seasons applicable to Phase 1 of aerobraking, they found that DK1 could generate wave-2 zonal structure in upper atmospheric density. These simulations predicted an increase in normalized wave-2 amplitude with increasing altitude up to 200 km at $L_s = 270°$, unlike the decrease observed between 130 km and 150 km at $L_s = 30$–$90°$ in Section 4.3, and essentially no phase change with increasing altitude. In later simulations applicable to the observations in Section 4.3, Forbes et al. (2001) predicted that the amplitude in temperature of DK1 should be constant with altitude between 120 km and 200 km. Since density at a given altitude is sensitive to the vertically integrated temperature below it, this implies that the normalized wave-2 amplitude in the density should increase from 120 km to 200 km.

Wilson has performed a series of tidal simulations (Wilson and Hamilton, 1996; Wilson, 2000, 2002). Wilson and Hamilton (1996) found that the $\sigma = 1$, $s = -1$, $n = 1$ Hough mode (DK1) had twice its usual amplitude during $L_s = 60$–$150°$, a period which includes the end of Phase 2 of aerobraking. This may contribute to the noticeable increase in the normalized wave-2 amplitude south of 15°N latitude in Fig. 8 which is coincident with the arrival of $L_s = 60°$, though simulations also show increasing amplitude to the south at fixed season (Wilson, 2000). In a comparison of TES temperatures with GCM results using a vertically averaged temperature with a broad weighting centred on 25 km altitude, Wilson (2000) found that stationary waves, but not tides, are too confined in latitude to cause planet-wide zonal structure, that diurnal tides made larger contributions than semidiurnal tides, and that each diurnal period, eastward propagating tidal mode had a deep vertical and broad meridional structure consistent with being dominated by the first symmetric Hough mode.

In simulations at 120 km altitude, Wilson (2002) found that the wave-2 zonal structure in the upper atmosphere was predominantly due to the $\sigma = 1$, $s = -1$, $n = 1$ Hough mode (DK1), the wave-3 zonal structure was a combination of the $\sigma = 1$, $s = -2$, $n = 2$ Hough mode (DK2) and the $\sigma = 2$, $s = -1$ tidal mode, and that these two wavenumbers dominate. He found the wave-3 zonal structure dominated by the diurnal mode in the tropics and by the semidiurnal mode in the extra-tropics, though he cautioned that those results were sensitive to the (uncertain) details of damping in the model. The wave-3 zonal structure has been observed to be

dominated by semidiurnal tidal modes in high latitude observations by Bougher et al. (2001) and our Section 4.5. The simulated semidiurnal mode has little phase shift with changing altitude, the diurnal mode has more. Wilson did not address the wave-1 and wave-4 components of zonal structure. The $\sigma = 1, s = -1, n = 1$ Hough mode (DK1) provides a consistent description of the Viking surface pressure data, TES temperatures at 25 km, and the wave-2 zonal density structure at 130 km, and has also has been observed in IRIS data from Mariner 9 (Conrath, 1976; Wilson, 2002).

Banfield et al. (2000) analysed tidal signatures in TES retrievals of lower atmospheric temperatures up to an altitude of ~ 40 km and south of 30°S latitude at $L_s = 180$–$390°$ from Phase 1 of aerobraking and the Science Phasing Orbits. They examined the eight σ, s tidal modes with a σ, s, n Hough mode shown in Fig. 17 that could cause wave-1 or wave-2 zonal structure and found that the $\sigma = 1$, $s = -1$ tidal mode was largest, followed by the $\sigma = 1$, $s = 0$ tidal mode. The first of these two tidal modes is probably dominated by the $\sigma = 1$, $s = -1$, $n = 1$ Hough mode (DK1) discussed above. The second of these two tidal mode, which causes zonal wave-1 structure, was identified in Wilson's simulations of temperatures centred on 25 km as the dominant mode in the zonal wave-1 structure (Wilson, 2000). All of Banfield et al.'s tidal amplitudes suggested increases northward of 30°S. Smith et al. (2001a) presented TES data from the later mapping mission, but did not repeat Banfield et al.'s detailed analysis of the tidal modes. However, a mix of tidal modes is present in their data. Since we have found wave-3 to be a much greater contributor to the zonal structure in the upper atmosphere than wave-1, it would be interesting to repeat Banfield et al.'s work including wave-3 modes.

Banfield et al. (2003) have also analysed tidal signatures in TES retrievals from post-aerobraking data. Their Fig. 11 is probably dominated by the $\sigma = 1$, $s = -1$ tidal mode and the $\sigma = 1, s = -1, n = 1$ Hough mode (DK1). It shows a relatively weak amplitude during the season corresponding to Phase 2 aerobraking. Like our Fig. 10, it shows highest amplitudes at the equator and higher amplitudes in the southern hemisphere than in the northern hemisphere. The longitude of the maximum is ~ 40°E in their lower atmosphere data and ~ 80°E in our upper atmosphere data, suggesting phase changes with height. Their Fig. 12 is probably dominated by the $\sigma = 1$, $s = -2$ tidal mode and the $\sigma = 1$, $s = -2$, $n = 2$ Hough mode (DK2). This is restricted to the tropics in their observations and cannot be responsible for the strong wave-3 harmonic which we observe in the extra-tropics (our Fig. 11). In Banfield et al., the maximum amplitude of the $\sigma = 2$, $s = -1$ tidal mode is no more than half that of DK2. However, since it is not restricted to the tropics, it could be the strongest contributor to the wave-3 zonal harmonic in the upper atmosphere, which would be consistent with our observations of a semidiurnal tidal mode for this harmonic in the southern polar regions.

Unambiguous identification of a particular Hough mode in the martian atmosphere requires many observations. The zonal wavenumber and period of the disturbance must be measured using observations at varied longitudes and LSTs. The meridional profile of the disturbance must be measured using observations at varied latitudes. The vertical profile of the disturbance must be measured using observations at varied altitudes. Observations of the background state of the atmosphere must be used in conjunction with modeling work beyond the classical tidal theory to predict the behaviour of candidate Hough modes as they are generated at the surface and propagate upwards through the spatially and temporally varying lower atmosphere. We are not able to satisfy all these requirements in this paper. Our identifications of certain Hough modes in this paper are based primarily upon the observed density variations with longitude at fixed LST at many latitudes, the observed density variations with longitude near the South Pole at two LSTs half a sol apart, and classical tidal theory. These restrictions should be understood before the conclusions of this paper are accepted by the reader. We discuss ways to test our conclusions in Section 6.

In summary, our conclusion that the wave-2 zonal structure is attributable to the $\sigma = 1, s = -1, n = 1$ Hough mode (DK1) is consistent with much observational and theoretical work. Our conclusion that the wave-3 zonal structure is attributable to the $\sigma = 2$, $s = -1$, $n = 1$ Hough mode is consistent with theoretical work and observations at high latitudes, but theoretical work suggests that the $\sigma = 1$, $s = -2$, $n = 2$ Hough mode (DK2), which we rejected based on the observed phase change at high latitudes, may be important at low to mid-latitudes. Observational and theoretical work in the lower atmosphere predicts that the $\sigma = 1$, $s = 0$ tidal mode dominates the zonal wave-1 structure, but we rejected it as a major influence in the upper atmosphere due to its short vertical wavelength. There has been little work relevant to the wave-4 zonal structure. We make one modification to our preliminary conclusions from Section 5.1. Previously rejected, the $\sigma = 1$, $s = -2$, $n = 2$ Hough mode (DK2) may make a significant contribution to the wave-3 zonal structure in the tropics.

5.3. Effects of the surface on zonal structure

The zonal structure in the upper atmosphere must be caused by a zonal asymmetry in the lower boundary conditions of the atmosphere interacting with solar heating to excite a non-migrating tide. In this section we investigate which zonal asymmetry might have the strongest influence on the zonal structure.

Dust loading is variable on relatively short timescales, so it is unlikely to be responsible for the long-lasting, stable zonal structure. Information on the spatial distribution of dust is available from archived TES results, but recent publications have focused on the dust distribution during dust

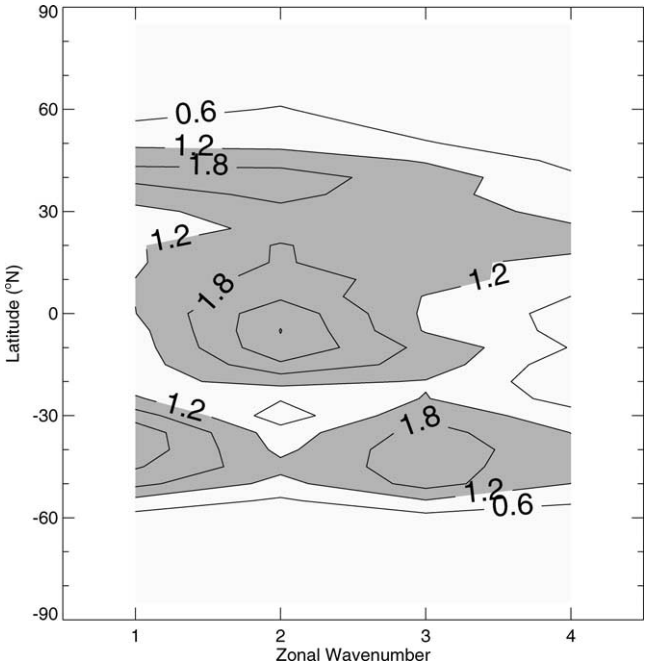

Fig. 18. Amplitudes, in km, of the various zonal harmonics in martian topography as a function of latitude. Contour intervals are 0.6 km and values greater than 1.2 km are shaded.

storms and not during the relatively calm period of Phase 2 of aerobraking (Smith et al., 2000, 2001a).

Continuing from Section 5.1, it seems reasonable that the meridional profile of the zonal asymmetry that, in conjunction with solar heating, can excite a given Hough mode must overlap significantly with the meridional profile of solar heating (peaked in the tropics, equatorially symmetric, and without any minima close to the equator) for that Hough mode to be efficiently excited. Using Mars Consortium data kindly supplied to us by Jim Murphy and MOLA topography, we performed harmonic decompositions of topography, thermal inertia, and albedo as a function of longitude at different latitudes (Smith et al., 2001b). As shown in Fig. 18, the wave-1 component of topography is low near the equator and highest in the extra-tropics. The wave-2 component of topography has high amplitudes throughout the tropics, is greatest at the equator, and decreases into the extra-tropics. Except for a narrow region of low amplitude at 30°S, it is reasonably symmetric about the equator. The wave-3 component has high amplitude at the equator, is quite constant throughout the tropics and decreases rapidly poleward of 60°. The wave-4 component of topography is low near the equator and highest in the extra-tropics. All amplitudes are below 0.6 km in smooth terrain poleward of 60°. The wave-2 and wave-3 components of topography satisfy the overlap criteria, but none of the components of albedo or thermal inertia do. As discussed in Section 5.1, both these components of topography can generate Hough modes with the ability to propagate into the upper atmosphere and appear as wave-2 and wave-3 zonal structure. This is consistent with the observation in Section 4.4 that these harmonics are the strongest.

It has already been shown that topography, the range of which exceeds an atmospheric scale height, is the main cause of the $\sigma = 1$, $s = -1$, $n = 1$ Hough mode (DK1) (Wilson and Hamilton, 1996; Wilson, 2002). This justification for the dominance of wave-2 and wave-3 harmonics in the zonal structure is intended to offer some physical insight as a complement to the rigourous results of more complete models. It could be tested by repeating Wilson and Hamilton's work on the $\sigma = 1$, $s = -1$, $n = 1$ Hough mode (DK1) on the other Hough modes that are possible contributors to the zonal structure (Wilson and Hamilton, 1996).

6. Conclusions

Sol-to-sol variability, or weather, in the martian upper atmosphere is not well modeled by current climate models. As martian climate models develop into weather models with the goal of understanding and interpreting the results of current and anticipated long-term, global-scale, atmospheric monitoring from orbiting instruments with high spatial and temporal resolutions, this variability with short spatial and temporal scales at high altitudes will provide a challenging test of their abilities. This variability is also significant for the design of future aerobraking missions.

For the seasons and latitudes discussed here, the sol-to-sol variability at fixed longitude, altitude, latitude, LST, and season is smaller than the longitudinal variability at fixed altitude, latitude, LST, and season. This repeatable variation with longitude, or zonal structure, can cause densities to change by a factor of two or more over less than 90° of longitude. The zonal structure must be due to thermal tides generated at or near the planet's surface. It is remarkable that surface effects are so significant at altitudes of 150 km.

We have used the changes in the zonal structure with altitude, latitude, and LST, together with a simple application of classical tidal theory, to identify the tidal modes that have the strongest contributions to the zonal structure. The week-to-week stability of the zonal structure and its similar behaviour at all latitudes require a planetary scale, not localized, phenomenon. The $\sigma = 1$, $s = -1$, $n = 1$ (wave-2, DK1) and $\sigma = 2$, $s = -1$, $n = 1$ (wave-3) Hough modes have been identified as major contributors to the zonal structure and this is supported by previous theoretical work. The $\sigma = 1$, $s = -2$, $n = 2$ (wave-3, DK2) Hough mode is predicted to be present. The wave-4 component of the zonal structure is attributed to the $\sigma = 2$, $s = -2$, $n = 2$ Hough mode and the cause of the weak wave-1 component is uncertain. We have presented a simple justification, based on the meridional profiles of solar heating and of various harmonic components of topography, thermal inertia, and albedo, for why the wave-2 and wave-3 components dominate the zonal structure and suggested that both are controlled by topography.

We believe that our conclusions are robust, although, as discussed in Section 5.2, these Hough modes have been identified indirectly. The main ways in which they might

be tested are (a) observations of the zonal wavenumbers and periods of any zonal structure in the middle atmosphere which would test our conclusion that certain Hough modes are propagating through the middle atmosphere, (b) upper atmospheric observations at more varied longitudes and LSTs, which, by identifying the zonal wavenumbers and periods of the zonal structure, would test our identification of certain Hough modes in the upper atmosphere, and (c) detailed modeling work, which would test our simplified ideas about vertical propagation of Hough modes. For consistency, these new observations would be most useful if they occurred at the same L_s as the MGS accelerometer observations.

At the surface of the Earth, atmospheric tides are often small-scale fluctuations masked by the effects of weather and only detectable in long duration records. At higher altitudes, they are more prominent. On Mars, whose atmosphere has a greater diurnal variation in solar heating per unit mass than Earth's, tidal effects are greater. They are a major feature in the long-term pressure measurements at the two Viking landing sites and were predicted by the very first martian climate model (Leovy and Mintz, 1969; Zurek et al., 1992). Tides have long been recognized as a basic feature of the dynamics of the martian lower atmosphere; this work, and others, demonstrates that they are important in the upper atmosphere as well. As such, upper atmosphere models which do not have dynamic connections to lower atmosphere models will be unable to reproduce observations or make accurate predictions.

The strength of a tidal mode in the martian upper atmosphere depends on the winds and temperatures in the lower atmosphere. If surface-to-thermosphere models can reliably reproduce the upper atmosphere observations, then only those lower atmosphere conditions which correspond to the observed behaviour in the upper atmosphere are permissible. This offers a way to constrain the behaviour of the lower atmosphere using only observations from the upper atmosphere.

Accelerometers are the only scientific instruments that will fly again and again into Mars orbit during the next decade. As such, they offer a unique way to study the behaviour of the difficult-to-study upper atmosphere over interannual periods and the 11-year solar cycle. Their observations are difficult to compare to most current martian climate models because of their high altitude, and this partially explains why so few recent publications have discussed accelerometer data, but they still have value. Accelerometer datasets will be invaluable in the future when, inevitably, models reach such altitudes, and every opportunity should be taken now to collect and preserve such datasets.

Acknowledgments

We thank Don Banfield, Jeff Forbes, Jill Hanna, Jim Murphy, Bob Tolson, John Wilson, and an anonymous reviewer. The studies of Hough modes in Section 5.1 were performed using computer programs kindly provided by Jeff Forbes.

References

Albee, A.L., Pelluconi, F.D., Arvidson, R.E., 1998. Mars Global Surveyor Mission: overview and status. Science 279, 1671–1672.

Albee, A.L., Arvidson, R.E., Palluconi, F., Thorpe, T., 2001. Overview of the Mars Global Surveyor Mission. J. Geophys. Res. 106, 23291–23316.

Angelats i Coll, M., Forget, F., Hourdin, F., Wanherdrick, J., Lopez-Valverde, M.A., Lewis, S.R., Read, P.L., 2002. First results with the Mars thermospheric LMD general circulation model. EGS XXVII General Assembly. #EGS02-A-04418 (abstract).

Banfield, D., Conrath, B.J., Pearl, J.C., Smith, M.D., Christensen, P.R., 2000. Thermal tides and stationary waves on Mars as revealed by Mars Global Surveyor thermal emission spectrometer. J. Geophys. Res. 105, 9521–9537.

Banfield, D., Conrath, B.J., Smith, M.D., Christensen, P.R., Wilson, R.J., 2003. Forced waves in the martian atmosphere from MGS TES Nadir data. Icarus 161, 319–345.

Bougher, S.W., Keating, G.M., Zurek, R.W., Murphy, J.M., Haberle, R.M., Hollingsworth, J., Clancy, R.T., 1999. Mars Global Surveyor aerobraking: atmospheric trends and model interpretation. Adv. Space Res. 23 (11), 1887–1897.

Bougher, S.W., Engel, S., Hinson, D.P., Forbes, J.M., 2001. Mars Global Surveyor radio science electron density profiles: neutral atmosphere implications. Geophys. Res. Lett. 28, 3091–3094.

Bougher, S.W., Murphy, J.R., Engel, S., 2002. Coupling processes and model simulations linking the Mars lower and upper atmospheres. 34th COSPAR Scientific Assembly, #A-00132 (abstract).

Cancro, G.J., Tolson, R.H., Keating, G.M., 1998. Operational data reduction procedure for determining density and vertical structure of the martian upper atmosphere from Mars Global Surveyor accelerometer measurements. NASA/CR-998-208721 and Master's thesis, Joint Institute for Advanced Flight Studies, George Washington University and NASA Langley Research Centre, October 1998.

Chapman, S., Lindzen, R.S., 1970. Atmospheric Tides. Gordon and Breach, New York.

Conrath, B.J., 1976. Influence of planetary-scale topography on the diurnal thermal tide during the 1971 martian dust storm. J. Atmos. Sci. 33, 2430–2439.

Croom, C.A., Tolson, R.H., 1994. Using Magellan attitude control data to study the venusian atmosphere and various spacecraft properties. Adv. Astronaut. Sci. 87, 451–467.

Eldred, C.H., 1991. Aerobraking for space exploration. In: Mars: Past, Present, and Future; Proceedings of the Conference, Williamsburg, VA (July 16–19, 1991). American Institute of Aeronautics and Astronautics, pp. 307–322.

Forbes, J.F., 1995. Tidal and planetary waves. In: Johnson, R.M., Killeen, T.L. (Eds.), The Upper Mesosphere and Lower Thermosphere: a Review of Experiment and Theory. American Geophysical Union, Washington, pp. 67–87.

Forbes, J.F., Hagan, M.E., 2000. Diurnal Kelvin wave in the atmosphere of mars: towards an understanding of "stationary" density structures observed by the MGS accelerometer. Geophys. Res. Lett. 27, 3563–3566.

Forbes, J.F., Makarov, N.A., Portnyagin, Y.I., 1995. First results from the meteor radar at South-Pole—a large 12-hour oscillation with zonal wave-number one. Geophys. Res. Lett. 22, 3247–3250.

Forbes, J.F., Gonzalez, R., Marcos, F.A., Revelle, D., Parish, H., 1996. Magnetic storm response of lower thermosphere density. J. Geophys. Res. 101, 2313–2319.

Forbes, J.M., Palo, S.E., Marcos, F.A., 1999. Longitudinal structures in lower thermosphere density. J. Geophys. Res. 104, 4373–4385.

Forbes, J.M., Hagan, M.E., Bougher, S.W., Hollingsworth, J.L., 2001. Kelvin wave propagation in the upper atmospheres of Mars and Earth. Adv. Space Res. 27 (11), 1791–1800.

French, J.R., Uphoff, C.W., 1979. Aerobraking for planetary missions, American Astronautical Society paper 79, p. 286.

Hinson, D.P., Tyler, G.L., Hollingsworth, J.L., Wilson, R.J., 2001. Radio occultation measurements of forced atmospheric waves on Mars. J. Geophys. Res. 106, 1463–1480.

Hollingsworth, J.L., Barnes, J.R., 1996. Forced, stationary planetary waves in Mars' winter atmosphere. J. Atmos. Sci. 53, 428–448.

Hooke, W.H., 1977. Rossby-planetary waves, tides, and gravity waves in the upper atmosphere. In: The Upper Atmosphere and Magnetosphere. National Research Council Studies in Geophysics, Washington, pp. 130–140.

Joshi, M.J., Hollingsworth, J.L., Haberle, R.M., Bridger, A.F.C., 2000. An interpretation of Martian thermospheric waves based on analysis of a general circulation model. Geophys. Res. Lett. 27, 613–616.

Keating, G.M., Taylor, F.W., Nicholson, J.Y., Hinson, E.W., 1979. Short-term cyclic variations and diurnal variations of the Venus upper atmosphere. Science 205, 62–64.

Keating, G.M., et al., 1998. The structure of the upper atmosphere of Mars: in situ accelerometer measurements from Mars Global Surveyor. Science 279, 1672–1676.

Keating, G.M., Tolson, R.H., Noll, S.N., Schellenberg, T.J., Stephens, R.L., Bradford, M.S., Bougher, S.W., Hollingsworth, J.L., 1999. First global mapping of the Mars thermosphere. Bull. Am. Astron. Soc. 31, #76.02 (abstract).

Keating, G.M., Dwyer, A., Wilson, R.J., Tolson, R.H., Bougher, S.W., Withers, P.G., Forbes, J.M., 2000. Evidence of large global diurnal Kelvin wave in Mars upper atmosphere. Bull. Am. Astron. Soc. 32, #50.02 (abstract).

Keating, G.M., Tolson, R.H., Hanna, J.L., Beebe, R.F., Murphy, J.R., Huber, L.F., 2001a. MGS-M-ACCEL-5-PROFILE-V1.1. NASA Planetary Data System.

Keating, G.M., Tolson, R.H., Hanna, J.L., Beebe, R.F., Murphy, J.R., Huber, L.F., 2001b. MGS-M-ACCEL-5-ALTITUDE-V1.0. NASA Planetary Data System.

Leovy, C.B., Mintz, Y., 1969. Numerical simulation of the atmospheric circulation and climate of Mars. J. Atmos. Sci. 26, 1167–1190.

Lyons, D.T., 1999. Aerobraking at Venus and Mars: a comparison of the Magellan and Mars global surveyor aerobraking phases. Am. Astron. Soc., 99–358.

Lyons, D.T., Saunders, R.S., Griffith, D.G., 1995. The Magellan Venus mapping mission: aerobraking operations. Acta Astronautica 35, 669–676.

Marcos, F.A., Garrett, H.B., Champion, K.S.W., Forbes, J.M., 1977. Density variations in lower thermosphere from analysis of AE-C accelerometer measurements. Planet. Space Sci. 25 (5), 499–507.

Murphy, J.R., Martin, T.Z., Blackmon, M., Nelli, S., 2001. Quantification of high frequency thermal waves in the martian atmosphere: analysis of MGS Horizon Sensor atmospheric temperatures. Bull. Am. Astron. Soc. 33, #19.23 (abstract).

Murray, C.D., Dermott, S.F., 1999. Solar System Dynamics. Cambridge University Press, Cambridge, Great Britain.

Neter, J., Wasserman, W., 1974. Applied Linear Statistical Models. Irwin, Homewood, IL.

Smith, M.D., Pearl, J.C., Conrath, B.J., Christensen, P.R., 2000. Mars global surveyor thermal emission spectrometer (TES) observations of dust opacity during aerobraking and science phasing. J. Geophys. Res. 105, 9539–9552.

Smith, M.D., Pearl, J.C., Conrath, B.J., Christensen, P.R., 2001a. Thermal emission spectrometer results: Mars atmospheric thermal structure and aerosol distribution. J. Geophys. Res. 106, 23929–23946.

Smith, D.E., et al., 2001b. Mars orbiter laser altimeter: experiment summary after the first year of global mapping of Mars. J. Geophys. Res. 106, 23689–23722.

Stewart, A.I.F., 1987. Revised time dependent model of the martian atmosphere for use in orbit lifetime and sustenance studies. LASP-JPL Internal Report, PO# NQ-802429, Jet Propulsion Lab., Pasadena.

Strangeway, R.J., 1993. The Pioneer Venus orbiter entry phase. Geophys. Res. Lett. 20, 2715–2717.

Tolson, R.H., Keating, G.M., Cancro, G.J., Parker, J.S., Noll, S.N., Wilkerson, B.L., 1999. Application of accelerometer data to Mars Global Surveyor aerobraking operations. J. Spacecraft Rockets 36 (3), 323–329.

Tolson, R.H., Keating, G.M., Noll, S.N., Baird, D.T., Shellenberg, T.J., 2000. Utilization of Mars Global Surveyor accelerometer data for atmospheric modeling. Adv. Astronaut. Sci. 103, 1329–1346.

Tracadas, P.W., Zuber, M.T., Smith, D.E., Lemoine, F.G., 2001. Density structure of the upper thermosphere of Mars from measurements of air drag on the Mars Global Surveyor spacecraft. J. Geophys. Res. 106, 23349–23358.

Wilson, R.J., 2000. Evidence for diurnal period Kelvin waves in the martian atmosphere from Mars Global Surveyor TES data. Geophys. Res. Lett. 27, 3889–3892.

Wilson, R.J., 2002. Evidence for nonmigrating thermal tides in the Mars upper atmosphere from the Mars Global Surveyor accelerometer experiment. Geophys. Res. Lett. 29 (7), 10.1029/2001GL013975.

Wilson, R.J., Hamilton, K., 1996. Comprehensive model simulation of thermal tides in the martian atmosphere. J. Atmos. Sci. 43, 1290–1326.

Withers, P., Bougher, S.W., Keating, G.M., 2000. New results from Mars Global Surveyor accelerometer. Lunar Planet. Sci. Conf. XXXI, #1268 (abstract).

Zurek, R.W., Barnes, J.R., Haberle, R.M., Pollack, J.B., Tillman, J.E., Leovy, C.B., 1992. In: Kieffer, H.H., Jakosky, B.M., Snyder, C.W., Matthews, M.S. (Eds.), Dynamics of the Atmosphere of Mars. Mars. Univ. of Ariz. Press, Tucson, pp. 835–933.